Ru(II) Phenanthroline-Based Oligothienyl Complexes as Phototherapy Agents

Houston D. Cole,^a Abbas Vali,^a John A. Roque III,^{a,b} Ge Shi,^a Gurleen Kaur,^a Rachel O. Hodges,^b Antonio Francés-Monerris,^c Marta E. Alberto,^{d*} Colin G. Cameron,^{a*} Sherri A. McFarland^{a*}

- ^a Department of Chemistry and Biochemistry, The University of Texas at Arlington, Arlington, Texas, 76019-0065 USA
- ^b Department of Chemistry and Biochemistry, The University of North Carolina at Greensboro, Greensboro, North Carolina 27402 USA
- c Institut de Ciència Molecular, Universitat de València, 46071 València, Spain
- ^d Dipartimento di Chimica e Tecnologie Chimiche, Università della Calabria, Arcavacata di Rende, 87036 Italy
- *Corresponding authors: C.G.C. <colin.cameron@uta.edu> ORCID 0000-0003-0978-0894, S.A.M. <sherri.mcfarland@uta.edu> ORCID 0000-0002-8028-5055

1 ABSTRACT

Ru(II) polypyridyl complexes have gained widespread attraction as photosensitizers for photodynamic therapy (PDT). Herein, we systematically investigate a series of the type $[Ru(phen)_2(IP-nT)]^{2+}$, featuring 1,10-phenanthroline (phen) coligands and imidazo[4,5-f][1,10]phenanthroline ligands tethered to n= 0-4 thiophene rings (IP-nT). The complexes were characterized and investigated for their electrochemical, spectroscopic, and (photo)biological properties. The electrochemical oxidation of the nT unit shifted by -350 mV as $n=1\rightarrow 4$ (+920 mV for **Ru-1T**, +570 mV for **Ru-4T**); nT reductions were observed in complexes Ru-3T (-2530 mV) and Ru-4T (-2300 mV). Singlet oxygen quantum yields ranged from 0.53-0.88, with Ru-3T and Ru-4T being equally efficient (~0.88). The time-resolved absorption spectra of Ru-0T-1T were dominated by metal-to-ligand charge transfer (³MLCT) states (τ_{TA}=0.40–0.85 μs), but long-lived intraligand charge transfer (3ILCT) states were observed in Ru-2T-4T (TTA=25-148 µs). The 3ILCT energies of Ru-3T and Ru-4T were computed to be 1.6 eV and 1.4 eV, respectively. Phototherapeutic efficacy against melanoma cells (SK-MEL-28) under broad-band visible light (400-600 nm) increases as $n=0\rightarrow 4$: **Ru-0T** was inactive up to 300 μ M, **Ru-1T–2T** were moderately active (EC₅₀ ~600 nM, PI=200), and Ru-3T (EC₅₀=57 nM, PI=>1100) and Ru-4T (EC₅₀=740 pM, PI=114,000) were the most phototoxic. Activity diminishes with longer wavelengths of light and is completely suppressed for all complexes except Ru-3T and Ru-4T in hypoxia. Ru-4T is the more potent and robust PS in 1% O₂ over seven biological replicates (avg EC₅₀=1.3 μm, avg PI=985). **Ru-3T** exhibited hypoxic activity in five out of seven replicates, underscoring the need for biological replicates in compound evaluation. Singlet oxygen sensitization is likely responsible for phototoxic effects of the compounds in normoxia, but the presence of redox-active excited states may facilitate additional photoactive pathways for complexes with 3 or more thienyl groups. The ³ILCT state with its extended lifetime (30–40x longer than the ³MLCT state for **Ru-3T** and **Ru-4T**) implicates its predominant role in photocytotoxicity.

Keywords: Ruthenium polypyridyl complexes, photosensitizers, photobiology, photodynamic therapy, metal-to-ligand charge transfer (MLCT), intraligand charge-transfer (ILCT), ligand-to-ligand charge transfer (LLCT), melanoma, phenanthroline (phen), hypoxia

2 INTRODUCTION

Cancer remains the second most common cause of death globally, surpassed only by cardiovascular disease.¹ Despite significant advancements in treatment over the past few decades, particularly in the realms of immunotherapy^{2–4} and targeted therapy,^{5,6} there remains a pressing need for novel treatments and adjuvant therapies to complement surgery, radiation, and chemotherapy. In this regard, light-driven treatment modalities present a compelling alternative.

Photodynamic therapy (PDT) represents a unique and promising approach to targeted cancer treatment, which leverages a nontoxic photosensitizer (PS), benign light, and molecular oxygen to generate cytotoxic reactive oxygen species (ROS) for destroying tumors. PDT offers the advantage of localized intervention and minimal invasiveness, yielding fewer adverse effects and enhanced patient quality of life.^{7,8}

PDT leverages two layers of precision: (1) the selective uptake and retention of PSs in malignant tissues and (2) the use of light to trigger toxicity. The result is that phototoxicity is confined to regions where the PS, light, and oxygen overlap spatiotemporally. The PDT effect can be maximized by optimization of the light regimen, including wavelength, fluence, irradiance, and dosimetry as well as the drug-to-light interval (DLI).

The intrinsic reliance of PDT on oxygen to generate ROS is problematic for treating hypoxic tumours. In addition, PDT can induce hypoxia as oxygen is consumed during irradiation.^{9,10} Decreased generation of ROS limits the damage to cancerous cells. To address this, there is motivation to develop light-triggered compounds that exploit oxygen-independent mechanisms for phototoxicity.^{11–59} In this context, metal complexes such as Ru(II) polypyridyl systems have attracted considerable attention.^{7,11,13,60–73} Judicious choice of ligand-metal combinations provides access to access a variety of excited state configurations with characteristic photophysical properties and reactivities. Strategies have included photorelease of bulky ligands to reveal phototoxic metals and/or ligands,^{11,15,21,22,63,74–77} photocaging of chemotherapeutics and enzyme inhibitors,^{13,14,16,71,74,78–95} photoredox reactions,^{96,97} and increasing ROS yields (to maintain ¹O₂ generation at low oxygen tension).^{23,24,63}

Our group has a longstanding interest in metal complexes as PSs, not just for alternate modes of action. Their modular architectures and straightforward assembly allow rapid tuning of physicochemical, photophysical, and biological properties, which facilitates our tumor-centered approach to PS design. Our guiding premise is that an ideal PS does not exist, and PS design and optimization should consider the specific application. Our TLD1433, a terthienyl-containing Ru(II) polypyridyl complex, is exemplary and is currently in Phase II clinical trials for treating non-muscle invasive bladder cancer (NMIBC) with PDT (Clinicaltrials.gov identifier NCT03945162).^{7,98} It has a high quantum yield for ¹O₂ generation and is phototoxic toward cancer cells with minimal dark toxicity. It is preferentially activated in the clinic with green light to avoid any damage to underlying muscle tissue.

To better understand the properties of oligothiophene-based metal complexes such as TLD1433, and to also develop additional PSs, we are exploring different metal ions, coligands, thienyl groups, counter ions, and coordination geometries. 7,15,23,24,63,76,99 The longer-term goal is to establish structure-activity relationships (SARs) for photoactive oligothiophene-containing metal complexes that consider their physicochemical, photophysical, electrochemical, and biological characteristics. We are motivated by the remarkable activities of some of these complexes containing longer thienyl chains. In this study, we describe a new family of Ru(II) PSs bearing two ancillary 1,10-phenanthroline (phen) ligands and an imidazo[4,5-f][1,10]phenanthroline (IP) ligand tethered to thienyl groups (nT) with n=0–4. The five members of the [Ru(phen)₂(IP-nT)]²⁺ family and the reference compound [Ru(phen)₃]²⁺ were investigated

for their photocytotoxic effects toward melanoma cells using different wavelengths of light in normoxia and in hypoxia. Their lipophilicities, ground state absorption and emission properties, excited state configurations and lifetimes, and redox characteristics are systematically compared. The study provides a framework for understanding photophysical properties and biological activities, offering a robust platform to probe the fundamental dynamics that underpin PDT efficacy across a variety of oligothiophene-containing metal complexes with future biological studies. It also introduces two new hypoxia-active PSs that could be further developed.

3 MATERIALS AND METHODS

All complexes in this series were thoroughly characterized synthetically, spectroscopically, electrochemically, and (photo)biologically. Additional procedural details and characterization data may be found in the Supplementary Information.

3.1 Instrumentation.

Microwave reactions were performed in a CEM Discover microwave reactor. NMR spectra were collected using a JEOL ECA 500 NMR spectrometer (1 H) at UNCG's NMR facility or Agilent 700 MHz NMR spectrometer (1 H, 1 H– 1 H COSY, 13 C– 1 H HSQC, 13 C– 1 H HMBC) at the Joint School of Nanoscience and Nanoengineering (JSNN). ESI mass spectra were obtained using a Thermo Fisher LTQ Orbitrap XL coupled to a Water's Acquity Ultra-high Performance Liquid Chromatography (UPLC) stack using a BEH C18 column at UNCG's Triad Mass Spectrometry facility. HPLC analyses were carried out on an Agilent/Hewlett Packard 1100 series instrument (ChemStation Rev. A. 10.02 software) using a Hypersil GOLD C18 column (Thermo 25005-254630, guard 25003-014001) with an A–B gradient (40 min run; 2 M \rightarrow 95% B; A=0.1% formic acid in H₂O, B=0.1% formic acid in MeCN). Reported retention times are accurate to within $^{\pm}$ 0.1 min. Flash chromatography relied on the Teledyne Isco CombiFlash EZ Prep system with Silicycle SiliaSep silica flash cartridges (FLH-R10030B-ISO25).

3.2 Synthesis and Characterization

To the best of our knowledge, **Ru-0T–Ru-4T** have not been previously published. [Ru(phen)₃](Cl)₂ was synthesized using a modified literature procedure¹⁰⁰ that is described in detail below. Unless otherwise specified, all reagents and solvents were purchased from commercial sources and used without further purification. Water used for all biological experiments was deionized to a resistivity ≥ 18.2 MΩ using either a Barnstead or Milli-Q® filtration system. Ru(phen)₂Cl₂•2H₂O¹⁰¹ and IP-based ligands¹⁰² were prepared according to adapted literature procedures. The synthesis of IP-based ligands follows that described below for IP-4T. [2,2':5',2":5",2"'-quaterthiophene]-5-carbaldehyde (4T-CHO) was prepared as previously described.^{103,104} Final products are synthetically characterized in Figure S1–Figure S22 via ¹H NMR, ¹H– ¹H COSY NMR, HPLC, and ESI⁺–MS. **Ru-4T** required additional ¹³C, ¹³C–¹H HSQC, and ¹³C–¹H HMBC NMR experiments for full assignment of the quaterthiophene-containing complex (Figure S9–Figure S10). The CI⁻ salts of final complex products were obtained *via* anion metathesis on HCI-treated Amberlite IRA-410 resin with methanol as eluent and isolated in vacuo. Final complexes are a mixture of Δ/Λ isomers.

[Ru(phen)₃](Cl)₂. Ru(Cl)₃·~3H₂O (58 mg, 0.20 mmol) and 1,10-phenanthroline (115 mg, 0.64 mmol) was added to a microwave vessel containing argon-purged ethylene glycol (3 mL), then the mixture was subjected to microwave irradiation at 180°C for 15 min with stirring. The resulting dark red solution was then transferred to a separatory funnel with deionized water (25 mL) and CH₂Cl₂ (25 mL). After gentle agitation, the CH₂Cl₂ was drained, and the remaining aqueous layer was washed with CH₂Cl₂ until the CH₂Cl₂ layer was colorless (3x 25 mL portions). Then, CH₂Cl₂ (25 mL) and saturated aqueous KPF₆ (5 mL) was added, and the mixture was shaken gently. The CH₂Cl₂ layer was drained, and the product was

further extracted from the aqueous layer using CH_2Cl_2 until the aqueous layer was colorless (4x25 mL portions). The CH_2Cl_2 extracts were then combined and concentrated under reduced pressure. The product was then eluted from a silica gel flash column chromatography cartridge with a gradient of MeCN to 10% water in MeCN, followed by 7.5% water in MeCN with 0.5% KNO₃. The dark red, product-containing fractions, which eluted only in the presence of KNO₃, were then combined and concentrated under vacuum, then transferred to a separatory funnel with CH_2Cl_2 (25 mL), deionized water (25 mL), and saturated aqueous KPF_6 (1 mL). The resulting mixture was gently agitated and the CH_2Cl_2 layer was drained. Additional CH_2Cl_2 (2x25 mL portions) was used to extract the remaining product until the aqueous layer was colorless. The CH_2Cl_2 layers were then combined and dried under vacuum to yield $[Ru(phen)_3](PF_6)_2$, which was then converted to the corresponding Cl^- salt in quantitative yield using Amberlite IRA-410 with MeOH as the eluent, then purified further using Sephadex LH-20 with MeOH as the eluent, affording product $[Ru(phen)_3](Cl)_2$ as a dark red solid (107 mg, 58%). HNMR (700 MHz, MeOD- d_3 , ppm): δ 8.67 (d, J = 8.1 Hz, 6H, 4,7), 8.30 (s, 6H, 5,6), 8.10 (d, J = 5.2 Hz, 6H, 2,9), 7.70 (dd, J = 8.3, 5.2 Hz, 6H, 3,8). HRMS (ESI+) m/z for [M-2 Cl^- 12+ calcd: 321.0547; Found: 321.0547. HPLC retention time 9.27 min (99.5% purity by peak area).

[Ru(phen)₂(IP)](Cl)₂ (**Ru-0T**). Ru(phen)₂Cl₂·2H₂O (57 mg, 0.1 mmol) and IP (22 mg, 0.1 mmol) were added to a microwave vessel containing argon-purged ethylene glycol (4 mL) and subjected to microwave irradiation at 180°C for 15 min. The resulting dark red mixture was then isolated and purified in the same manner as [Ru(phen)₃](Cl)₂, yielding the desired product **Ru-0T** as a dark red solid (48 mg, 64%). ¹H NMR (700 MHz, MeOD- d_3 , ppm): δ 9.00 (broad s, 2H, c), 8.70 (d, J = 8.3 Hz, 4H. d_3 7), 8.67 (s, 1H, d_3 8), 8.33 (s, 4H, 5,6), 8.16 (dd, d_3 = 5.3, 1.3 Hz, 2H, 2), 8.11 (dd, d_3 = 5.2, 1.3 Hz, 2H, 9), 8.07 (dd, d_3 = 5.3, 1.3 Hz, 2H, d_3 8), 7.77 (dd, d_3 = 8.3, 5.3 Hz, 2H, d_3 9), 7.72 (m, 4H, 8,3). HRMS (ESI+) d_3 9 for [M-2Cl⁻]²⁺ calcd: 341.0578; Found: 341.0582. [M-2Cl⁻-H]⁺ calcd: 681.1084; Found: 681.1110. HPLC retention time: 9.07 min (98% purity by peak area).

[Ru(phen)₂(IP-1T)](Cl)₂ (**Ru-1T**). Ru(phen)₂Cl₂·2H₂O (57 mg, 0.1 mmol) and IP-1T (30 mg, 0.1 mmol) were added to a microwave vessel containing argon-purged ethylene glycol (4 mL) and subjected to microwave irradiation at 180°C for 15 min. The resulting dark red mixture was then isolated and purified in the same manner as compound [Ru(phen)₃](Cl)₂, yielding the desired product **Ru-1T** as a dark red solid (49 mg, 59%). ¹H NMR (700 MHz, MeOD- d_3 , ppm): δ 9.09 (broad s, 2H, c), 8.70 (dd, J = 8.4, 1.4 Hz, 4H, 4,7), 8.33 (s, 4H, 5,6), 8.18 (dd, J = 5.3, 1.3 Hz, 2H, 2), 8.12 (dd, J = 5.2, 1.3 Hz, 2H, 9), 8.05 (dd, J = 5.2, 1.3 Hz, 2H, a), 8.01 (dd, J = 3.7, 1.2 Hz, 1H, a), 7.76 (dd, J = 8.3, 5.3 Hz, 2H, a), 7.75 – 7.72 (m, 5H, a), 7.30 (dd, J = 5.1, 3.7 Hz, 1H, a). HRMS (ESI+) a0 for [M-2Cl⁻]²⁺ calcd: 382.0517; Found: 382.0523. [M-2Cl⁻-H]⁺ calcd: 763.0961; Found: 763.0974. HPLC retention time 10.62 min (99.5% purity by peak area).

[Ru(phen)₂(IP-2T)](Cl)₂ (**Ru-2T**). Ru(phen)₂Cl₂·2H₂O (57 mg, 0.1 mmol) and IP-2T (38 mg, 0.1 mmol) were added to a microwave vessel containing argon-purged ethylene glycol (4 mL) and subjected to microwave irradiation at 180°C for 15 min. The resulting dark red mixture was then isolated and purified in the same manner as compound [Ru(phen)₃](Cl)₂, yielding the desired product **Ru-2T** as a dark red solid (58 mg, 39%). ¹H NMR (700 MHz, MeOD- d_3 , ppm): δ 9.03 (broad s, 2H, c), 8.71 (d, J = 8.30, 4H, 4,7), 8.34 (s, 4H, 5,6), 8.21 (dd, J = 5.4, 1.3 Hz, 2H, 2), 8.12 (dd, J = 5.2, 1.3 Hz, 2H, 9), 8.05 (dd, J = 5.3, 1.3 Hz, 2H, a), 7.92 (d, J = 3.9 Hz, 1H, d), 7.78 – 7.71 (m, 6H, b,3,8), 7.44 (dd, J = 5.1, 1.2 Hz, 1H, f), 7.36 (d, J = 3.9 Hz, 1H, e), 7.33 (d, J = 3.5 Hz, 1H, h), 7.09 (dd, J = 5.1, 3.6 Hz, 1H, g). HRMS (ESI+) m/z for [M-2Cl⁻]²⁺ calcd: 423.0455; Found: 423.0458. [M-2Cl⁻-H]⁺ calcd: 845.0838; Found: 845.0852. HPLC retention time 21.19 min (99.5% purity by peak area).

 $[Ru(phen)_2(IP-4T)](CI)_2$ (Ru-4T). Ru(phen)₂Cl₂·2H₂O (114 mg, 0.2 mmol) and IP-4T (90 mg, 0.164 mmol) were added to a microwave vessel containing argon-purged ethylene glycol (4 mL) and subjected to microwave irradiation at 180°C for 15 min. The resulting dark red mixture was then isolated and purified in the same manner as compound [Ru(phen)₃](Cl)₂, yielding the desired product Ru-4T as a dark red solid (49 mg, 28%). ¹H NMR (700 MHz, MeOD- d_3 , ppm): δ 9.04 (s, 2H, c), 8.72 (d, J = 8.77 Hz, 2H, 4), 8.70 (d, J = 8.89 Hz, 2H, 7), 8.34 (s, 4H, 5,6), 8.22 (dd, J = 5.4, 1.3 Hz, 2H, 2), 8.12 (dd, J = 5.2, 1.3 Hz, 2H, 9), 8.05 (dd, J = 5.2, 1.3 Hz, 2H, a), 7.89 (d, J = 3.9 Hz, 1zH, d), 7.77 (dd, J = 8.2, 5.4 Hz, 2H, 3), 7.75 - 7.70 (m, 4H, 8,b), 7.33 (d, J = 3.9 Hz, 1H, e), 7.29 (dd, J = 5.1, 1.2 Hz, 1H, I), 7.24 (d, J = 3.7 Hz, 1H, f), 7.17 (dd, J = 3.6, 1.3 Hz, 1H, j), 7.12 (d, J = 3.8 Hz, 1H, h), 7.09 (d, J = 3.7 Hz, 1H, g), 7.04 (d, J = 3.8 Hz, 1H, h), 7.09 (d, J = 3.8 Hz, 1H, g), 7.04 (d, J = 3.8 Hz, 1H, h), 7.09 (d, J = 3.8 Hz, 1H, g), 7.04 (d, J = 3.8 Hz, 1H, h), 7.09 (d, J = 3.8 Hz, 1H, g), 7.04 (d, J = 3.8 Hz, 1H, h), 7.09 (d, J = 3.8 Hz, 1H, g), 7.04 (d, J = 3.8 Hz, 1H, h), 7.09 (d, J = 3.8 Hz, 1H, g), 7.04 (d, J = 3.8 Hz, 1H, h), 7.09 (d, J = 3.8 Hz, 1H, g), 7.04 (d, J = 3.8 Hz, 1H, h), 7.09 (d, J = 3.8 Hz, 1H, g), 7.04 (d, J = 3.8 Hz, 1H, h), 7.09 (d, J = 3.8 Hz, 1H, g), 7.04 (d, J = 3.8 Hz, 1H, h), 7.09 (d, J = 3.8 Hz, 1H, g), 7.04 (d, J = 3.8 Hz, 1H, g), 7.09 (d, J = 3.8 Hz, 1H, g), 7.04 (d, J = 3.8 Hz, 1H, g), 7.09 (d, J = 3.8 Hz, 1H, g), 7.04 (d, J = 3.8 Hz, 1H, g), 7.09 (d, J = 3.= 3.7 Hz, 1H, i), 7.00 (dd, J = 5.1, 3.5 Hz, 1H, k). ¹³C NMR (700 MHz, MeOD- d_3 , ppm): δ 153.96 (2), 153.77 (9), 151.57 (a), 150.08 (10), 149.29 (21), 149.19 (20), 147.36 (22), 141.46 (12), 138.31 (4,7,14), 138.14 (16), 137.78 (17), 136.36 (15), 136.24 (13), 132.57 (18), 132.54 (19), 131.89 (c, 11), 129.65 (d), 129.49 (6), 129.48 (5), 129.11 (k), 127.40 (8), 127.37 (3), 127.13 (b), 126.82 (f), 126.05 (l), 126.01 (h), 125.85 (e), 125.71 (g), 125.51 (i), 125.08 (j), HRMS (ESI+) m/z for [M-2Cl⁻]²⁺ calcd: 505.0333; Found: 505.0312. [M-2Cl-H]⁺ calcd: 1009.0593; Found: 1009.0663. HPLC retention time 23.92 min (99.5% purity by peak area).

3.3 Computational Details

The computational protocol used to investigate the Ru(II)-complexes herein presented is based on a combination of DFT and TDDFT 105 as methods as implemented in the Gaussian16 106 code and widely tested in previous studies involving metallic photosensitizers for PDT $^{107-114}$ and successfully adopted for our related Os(II)- and Ru-compounds. 23,24,63

The PBE0 exchange-correlation functional (XC)¹¹⁵ in conjunction with the 6-31+G(d,p) basis set was chosen for the singlet ground and lowest triplet excited states optimizations in water adopting the quasi-relativistic Stuttgart-Dresden pseudopotential to treat the Ru(II) center.¹¹⁶ The integral equation formalism polarizable continuum model^{117,118} (IEFPCM) was used to simulate the water solvent environment by using a dielectric constant equal to ε =80 by means of the polarizable conductor model (PCM).¹¹⁹

The M06 exchange-correlation (XC)-functional and the Tamm-Dancoff approximation (TDA) 120 were used to compute the UV-Vis absorption spectra in water on top of the corresponding S₀ equilibrium geometries. We recently adopted this method for optimizing the lowest triplet metal-to-ligand charge transfer (3 MLCT) and ligand-based mixed triplet intraligand charge transfer (3 LCT) / ligand-to-ligand charge transfer (3 LCT) excited states and computing the emission energies. The TDA circumvents the general underestimation of the triplet state energies from the conventional TDDFT approach, as was also observed in our earlier investigations on other oligothiophene-based Ru(II) and Os(II) complexes for

which the vertical lowest triplet excited states were underestimated.^{23,24,110} The nature of the excited states was determined in all cases by computing the corresponding natural transition orbitals (NTOs) with the Chemissian 4.67 software,¹²² and through Gaussian output post-processing conducted with the TheoDORE 3.1.1 program.¹²³

3.4 Electrochemistry

Voltammetry was performed in dimethylformamide (DMF, Fisher HPLC grade) that had been dried and deoxygenated with an Inert PureSolv MD7 solvent purification system, with 100 mM tetrabutylammonium hexafluorophosphate (TBAPF₆) (Fisher) as the supporting electrolyte, in a two-compartment low volume cell with the three-electrode configuration under argon. A 3 mm glassy carbon disc was used as the working electrode with a platinum wire counter electrode and a Ag/AgCl/4M KCl reference electrode. Ferrocene (Fc) was used as an internal standard. The complex solutions were approximately 4 mM for oxidation sweeps and 0.25 mM for reduction sweeps.

Measurements were conducted at room temperature using a WaveNow potentiostat (Pine Research Company) with Aftermath software. Cyclic differential-pulse voltammetry (CDPV) measurements used a sweep rate of 2 mV·s⁻¹ with a modulation amplitude varying from 12.5 to 100 mV. For reversible processes, the formal redox potential $E^{\circ\prime}$ was taken as the average of E_{pa} (anodic peak potential) and E_{pc} (cathodic peak potential). For quasi-reversible processes, only E_{pa} or E_{pc} is reported.

4 RESULTS AND DISCUSSION

4.1 Synthesis and Characterization

[Ru(phen)₃](Cl)₂ and **Ru-nT** were synthesized using our previously published method for related Ru(II) phenanthroline-based complexes.⁶³ The complexes were isolated as PF₆⁻ salts and purified using flash chromatography on silica. The PF₆⁻ salts were then converted to their corresponding Cl⁻ salts in quantitative yields via anion metathesis with Amberlite IRA-410 and further purified using size-exclusion chromatography on Sephadex LH-20. The final yields were ~60% for [Ru(phen)₃](Cl)₂, **Ru-0T**, **Ru-1T**, and **Ru-3T**, ~40% for **Ru-2T**, and ~30% for **Ru-4T**. The complexes were characterized by 1D and 2D ¹H NMR spectroscopy (Figure 1, Figure S1–Figure S10), with assignment of signals for [Ru(phen)₃](Cl)₂ and **Ru-0T–Ru-3T** made using ¹H–¹H COSY NMR. **Ru-4T** was additionally analysed by ¹H–¹³C HSQC and ¹H–¹³C HMBC NMR to assign the hydrogens of the quaterthiophene unit. The assignments were consistent with our related, previously reported compounds.^{23,63,76} The complexes were also

characterized by high-resolution ESI+ mass spectrometry (Figure S11–Figure S16). HPLC analyses indicated that the complexes were ≥95% pure by integration (Figure S17–Figure S22).

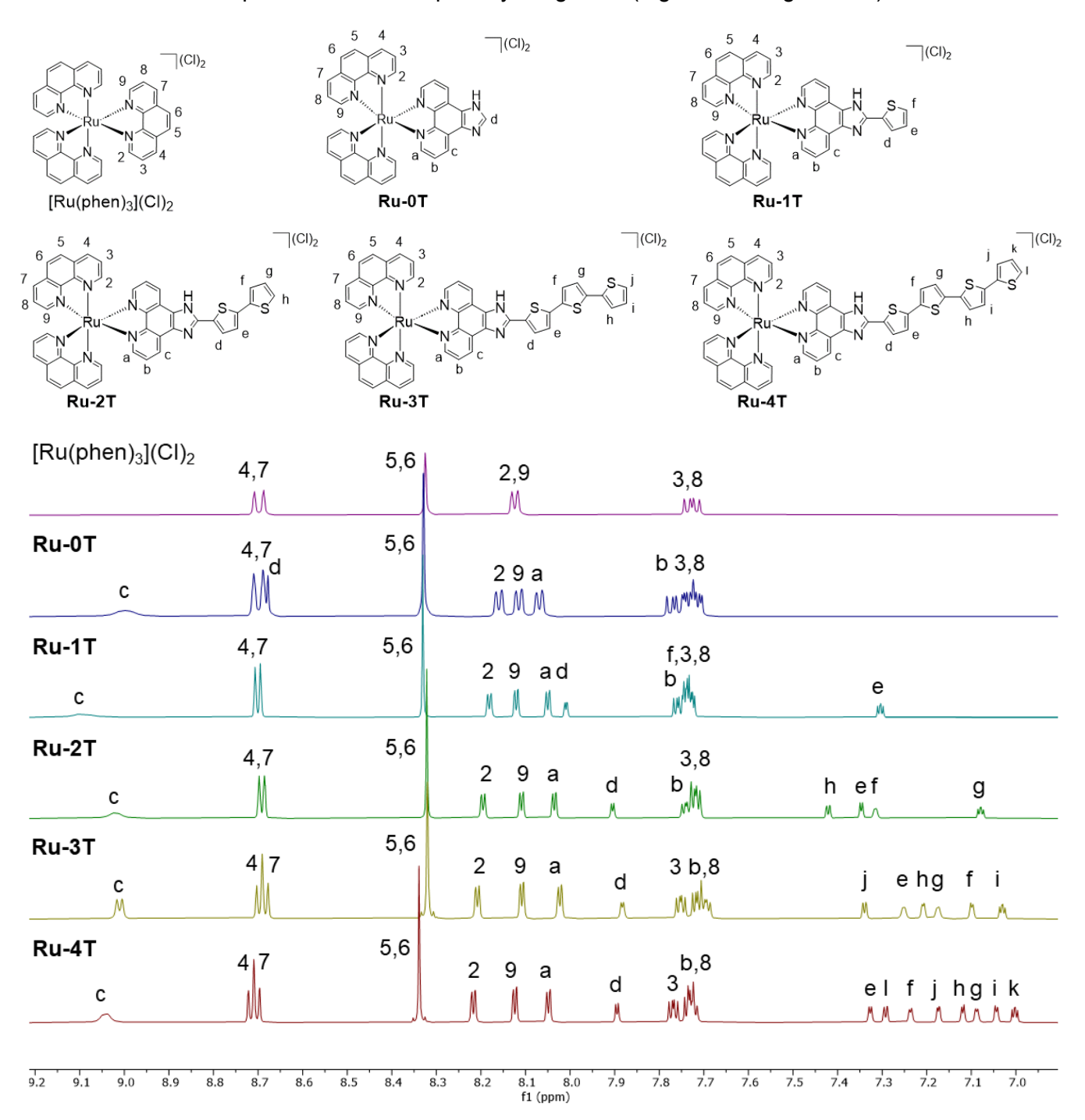


Figure 1. Aromatic region of the ${}^{1}H$ NMR spectra for [Ru(phen) ${}_{3}$](Cl) ${}_{2}$ and **Ru-nT** (n=0-4) in MeOD-d ${}_{3}$ (Cl ${}^{-}$ salts; 298 K). All spectra were collected at 500 MHz, except for **Ru-4T**, which was collected at 700 MHz.

The lipophilicities of $[Ru(phen)_3](Cl)_2$ and Ru-nT as their chloride salts were evaluated experimentally by calculating their log $D_{o/w}$ values from partitioning between 10 mM phosphate buffer solution (pH 7.4) and 1-octanol (99.9%) (Figure 2 and Table S1). A negative log $D_{o/w}$ value indicates hydrophilicity whereas a

positive log $D_{o/w}$ value indicates higher lipophilicity.¹²⁴ [Ru(phen)₃](Cl)₂ and **Ru-nT** up to n=2 were relatively hydrophilic overall, with log $D_{o/w}$ values becoming increasingly more positive with additional thiophene rings. An abrupt change in aqueous solubility occurred at n=3, with **Ru-3T** showing a clear preference for 1-octanol. **Ru-4T** also also preferred 1-octanol, but its log $D_{o/w}$ could not be determined due to precipitation between the two layers that left no measurable amount of compound in the aqueous phase. Precipitation at the octanol-buffer interface was also observed for the analogous Os(II) complex that self-associates in PBS to form particles of up to 1–2 μ m in diameter.²³ This is not uncommon for Ru(II) and Os(II) complexes containing the IP-4T ligand.

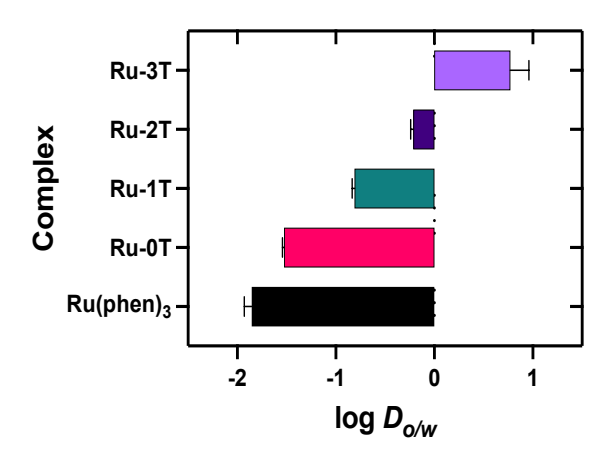


Figure 2. Lipophilicities of [Ru(phen)₃](Cl)₂ and **Ru-nT** (n=0–3) in 1-octanol and phosphate buffer using the shake-flask method. The log $D_{o/w}$ value for **Ru-4T** was undefined due to precipitation at the octanol:phosphate buffer interface that left no measurable amount of **Ru-4T** in the phosphate buffer phase.

4.2 Computation

<u>Singlet states.</u> Figure 3 shows the optimized singlet ground state structures of [Ru(phen)₃]²⁺ and **Ru-nT** (n=0–4) in water at the DFT/PBE0 level of theory, and the main geometric parameters are reported in Table S2 The central Ru(II) ion adopts an octahedral geometry with similar Ru-N bond distances across the series, with the first thiophene ring being coplanar with the coordinated IP ligand. Each subsequent ring introduces more conformational flexibility, with the fourth thienyl ring of **Ru-4T** being twisted out of plane by approximately 18°. The *n*T chain length has a major impact on the frontier orbitals. Similar to structurally related families we have reported, ^{23,24,63} complexes with $n \ge 2$ have progressively higherenergy HOMOs that give rise to a systematic reduction of the H-L gaps as the % *n*T contribution increases (Figure 4 and Figure S23, Table S3. The HOMO for **Ru-2T** extends over both the IP and *n*T unit, whereas the HOMOs are localized primarily to the *n*T chain for **Ru-3T** and **Ru-4T**, where the *n*T contribution to the HOMO is about 46% and 61%, respectively. In contrast, the LUMOs across the series are primarily phenbased (>95% for all complexes) and not affected significantly by *n*T.

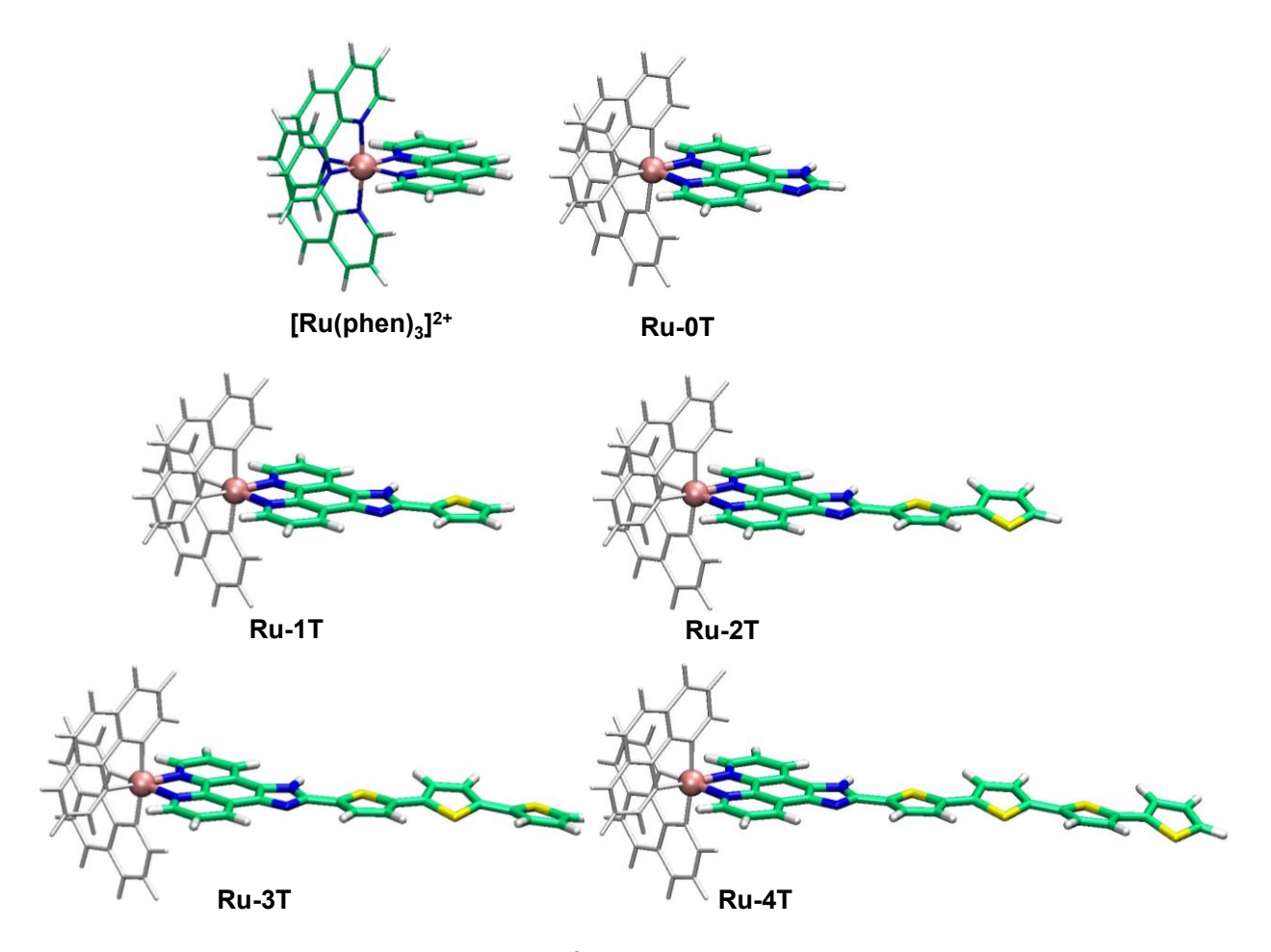


Figure 3. Optimized geometries of $[Ru(phen)_3]^{2+}$ and Ru-nT (n=0-4) in a water environment at the PBE0/6-31+G(d,p)/SDD/ level of theory. The two phen ligands are shown in grey for the Ru IP-nT complexes for the sake of clarity.

The computed lowest-energy, spin-allowed singlet-singlet absorption transitions shift to longer wavelengths with increasing n (Figure 5). The NTOs are predominantly 1 MLCT (Ru \rightarrow phen/IP) for [Ru(phen) $_3$] $^{2+}$, **Ru-0T** and **Ru-1T**. Their computed transitions are similar near 432–438 nm and slightly higher in energy than the experimental bands (vide infra). The lowest energy transitions for **Ru-2T**, **Ru-3T**, and **Ru-4T** are red-shifted with n, in agreement with experimental spectra. The lowest energy absorption was computed at 455 nm and was mixed 1 MLCT/ 1 LLCT character for **Ru-2T**. In the case of **Ru-3T** and **Ru-4T**, the lowest energy transitions were 1 ILCT/ 1 IL/ 1 LLCT character (mostly localized to the IP-nT ligand) and computed at 466 nm and 488 nm, respectively. **Ru-4T** has twice as much 1 ILCT/ 1 IL character compared to **Ru-3T**. Here, LLCT mainly refers to CT between nT and IP (but does include very minor involvement of the phen coligands); ILCT involves CT within nT; IL is $\pi\pi^*$ localized to nT or IP. Further details are summarized in Table S4 and Figure S24.

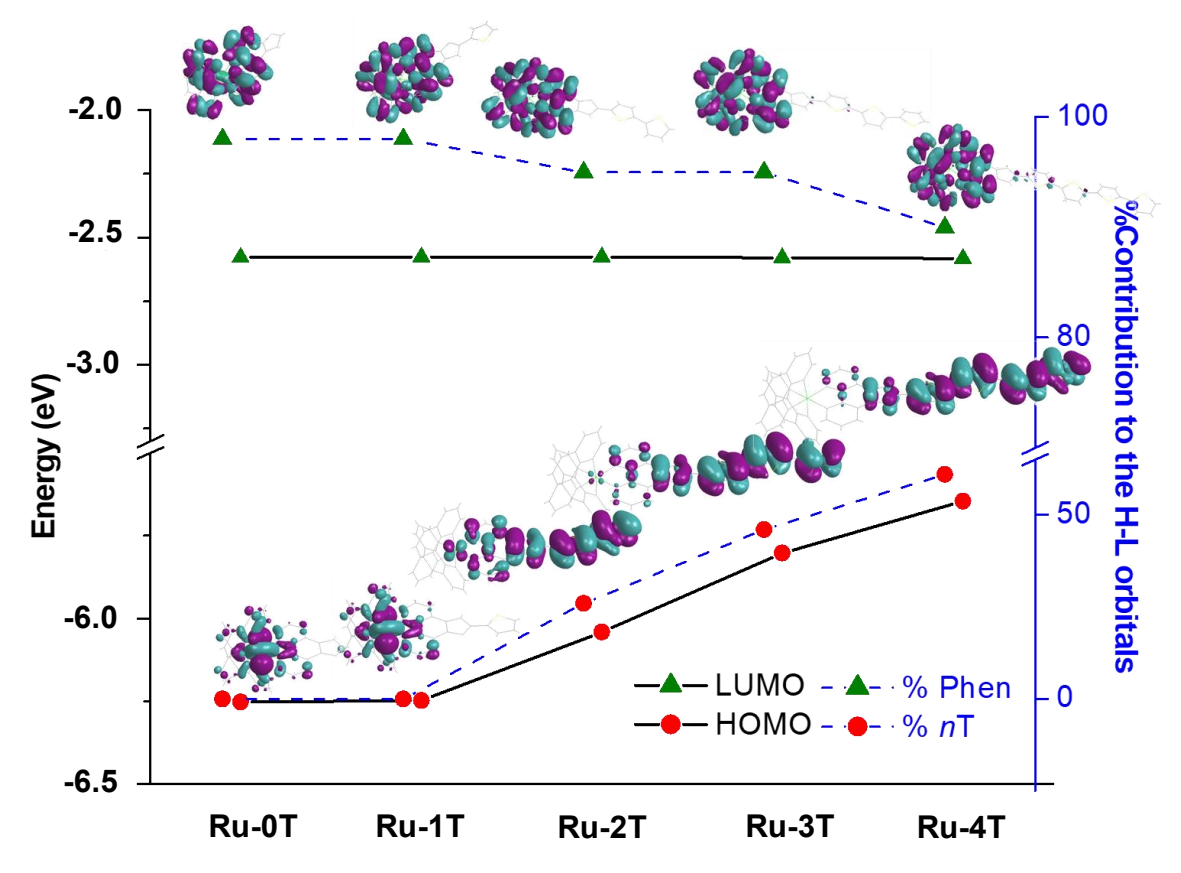


Figure 4. Computed HOMO and LUMO orbital energies (solid black lines) and percent contribution of the nT chain to the HOMO (dashed line, red filled circles) and of the phen coligands to the LUMO (dashed line, green filled triangles), for **Ru-n**T (n=0-4) in the singlet ground state, at the M06/6-31+G(d,p)/SDD level of theory, in water. Images of Ru(II)-based HOMOs for **Ru-0**T and **Ru-1**T, the nT-based HOMOs for n=2-4, and the phen-based LUMOs for all compounds, obtained at the same level of theory. Additional details can be found in Figure S23.

<u>Triplet states.</u> The optimized structures of the lowest excited triplet states (T_1) for the **Ru-nT** family involve a fully planar arrangement of the *n*T chain that maximizes the π-conjugation, with successive *n*T groups antiplanar to one another. The geometrical parameters of the T_1 states for $[Ru(phen)_3]^{2+}$ and Ru-nT (n=0-4) are listed in Table S2 alongside the data for S_0 , and the optimized T_1 state structures are shown in Figure S25. The lowest-energy triplet excited state configurations of this series are either 3 MLCT for complexes without thiophenes (or only one thiophene as in the case of **Ru-1T**) or mixed 3 ILCT/ 3 LLCT states for complexes with two or more thiophenes. The lowest-energy 3 MLCT states lie near 2.2 eV for all complexes in the series regardless of the thiophene chain length and whether the 3 MLCT state is T_1 . The energies of the mixed 3 ILCT/ 3 LLCT states depend on *n* and decrease systematically in energy from 1.82 eV for **Ru-2T** to 1.44 eV for **Ru-4T**. The triplet metal-centered (3 MC) and intraligand (3 IL) excited states localized to the phen/IP coligands are much higher in energy and contribute very little to the computed NTOs for T_1 . The energies and configurations of the computed triplet states are presented in Figure 6 and complied in Table 1 and Table S5. The occupied and virtual NTOs are plotted in Figure S26.

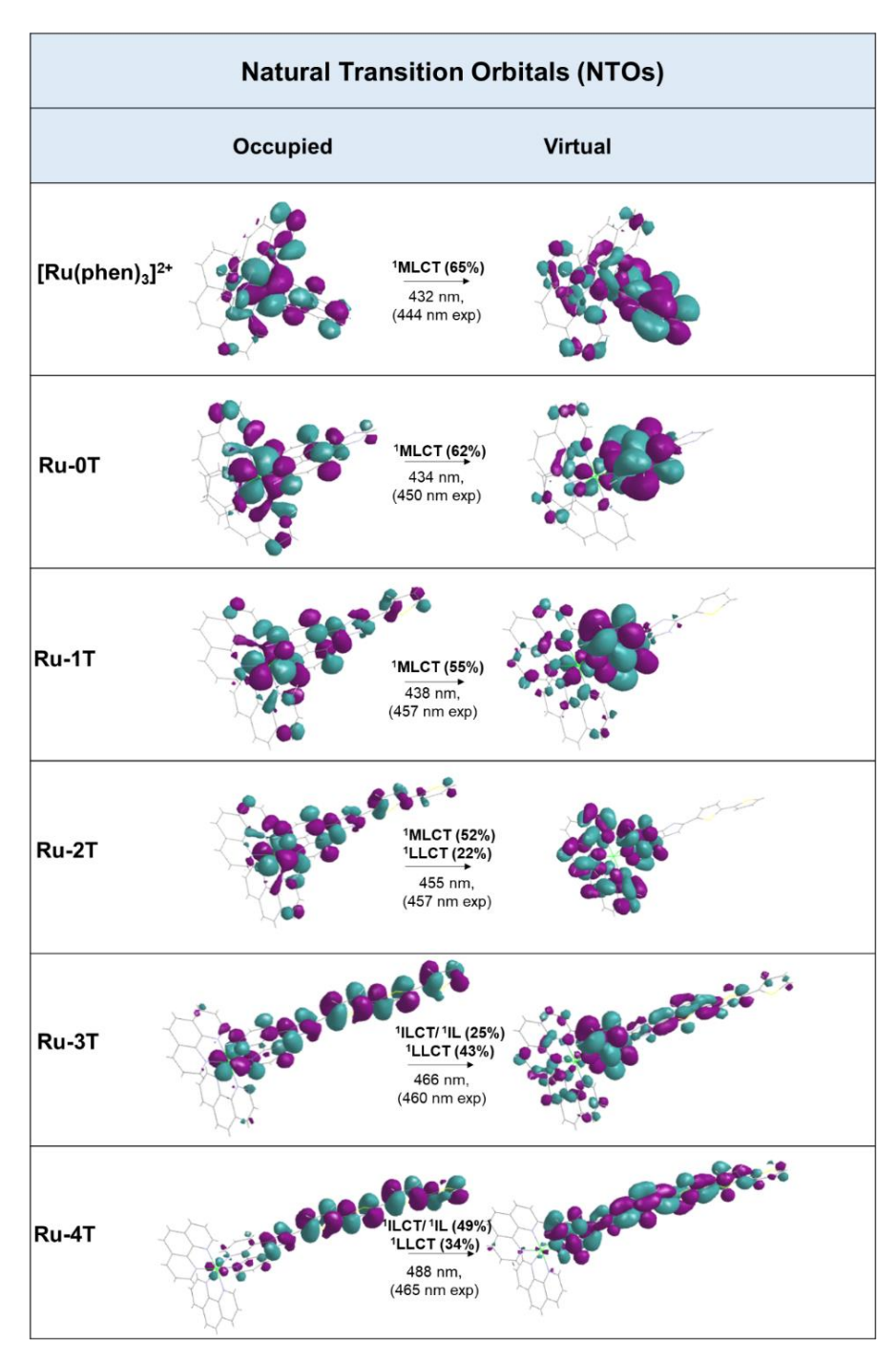


Figure 5. Occupied and Virtual NTOs of the computed lowest-energy singlet-singlet transitions in water (λ) with the predominant character indicated. The experimental longest wavelength absorption maxima (λ_{exp}) are reported in parentheses. Additional NTOs are reported in Figure S24.

Although the T₁ triplet state undergoes a significant drop in energy with increasing n, all are still sufficiently energetic to sensitize ${}^{1}O_{2}$. 125,126 Mulliken spin densities (MSD) close to 1 on the Ru(II) center further support that T₁ is predominantly ${}^{3}MLCT$ for [Ru(phen)₃]²⁺, **Ru-0T**, and **Ru-1T**. The MSD values of 0 on the Ru(II) center for complexes with $n \ge 2$ indicate that the metal is not involved in T₁. The predominant

Table 1. Computed T_1 adiabatic energies, configurations, and Mulliken spin densities (MSD) on the Ru(II) metal center for $[Ru(phen)_3]^{2+}$ and Ru-nT (n = 0-4). A single configuration is listed if that character was >50%.

	T₁ energy (eV)	Configuration	MSD	
[Ru(phen) ₃] ²⁺	2.21	3MLCT	0.86	
Ru-0T	2.18	3MLCT	0.86	
Ru-1T	2.18	³ MLCT	0.91	
Ru-2T	Ru-2T 1.82		0	
Ru-3T 1.57		³ ILCT	0	
Ru-4T	1.44	³ ILCT	0	

character of T₁ for **Ru-2T** is mixed 3 ILCT/ 3 LLCT, where 3 ILCT involves CT within the nT unit (nT $\rightarrow n$ T) and 3 LLCT involves CT between nT and IP (nT \rightarrow IP), and each contributes equally (\approx 40%) to the transition according to the topology analysis (Figure 6b). For **Ru-3T** and **Ru-4T**, T₁ is >50% 3 ILCT. The drop in T₁ energy on going from n=2 to 4 is accompanied by diminishing 3 LLCT character (from \sim 40% down to \sim 20%). Such behavior is in agreement with the related Ru(II) and Os(II) families we reported previously, 23,24,63 where T₁ involves the IP-nT ligand for n=2-4 and is increasingly more localized to the nT portion with increasing n. The higher-lying 3 MLCT state (T₂) for these complexes is similar in energy (\sim 2.2 eV) to those with n<2 having 3 MLCT states as T₁.

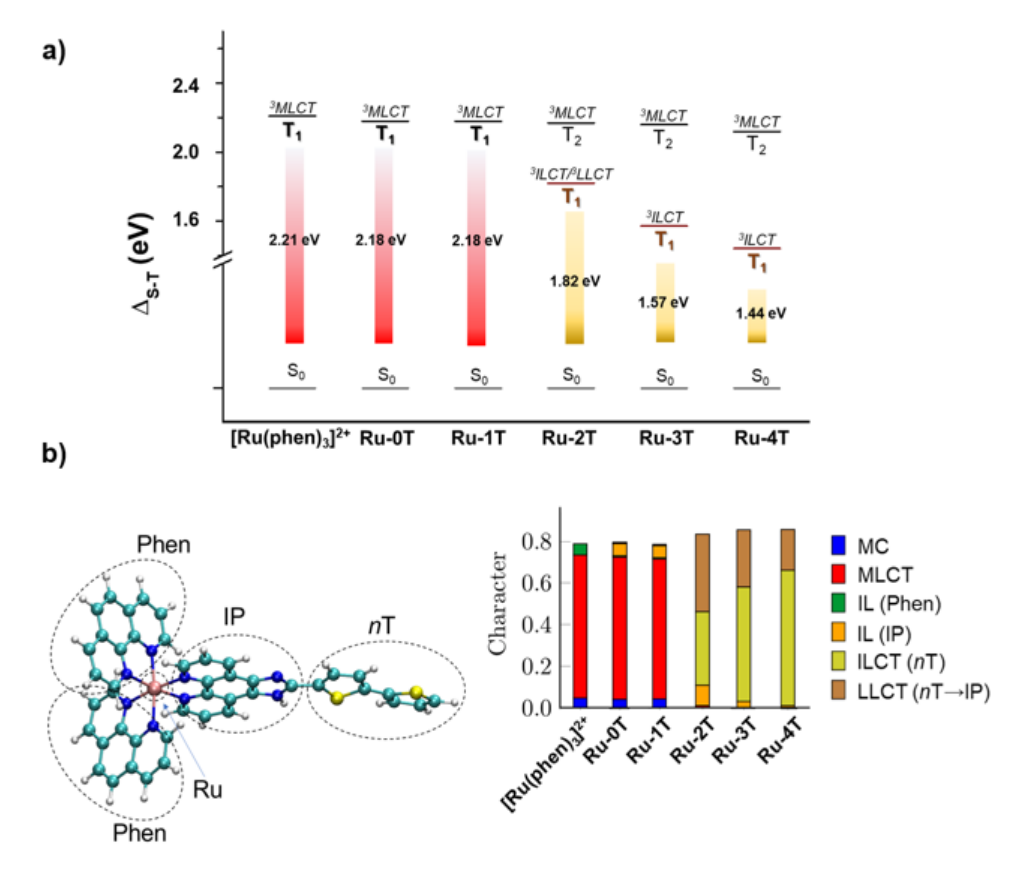


Figure 6. (a) Computed T_1 adiabatic energies for $[Ru(phen)_3]^{2+}$ and Ru-nT. (b) Molecular fragments (left) defined to quantify the molecular topology of the T_1 excited states and their configurations (right). The NTOs are reported in Figure S26 and triplet excited state energies in Table S5.

4.3 Spectroscopy

4.3.1 UV-Vis absorption and emission spectroscopy

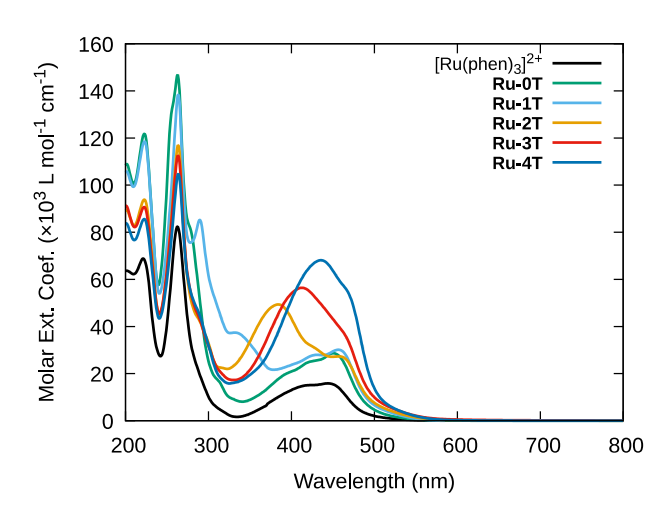


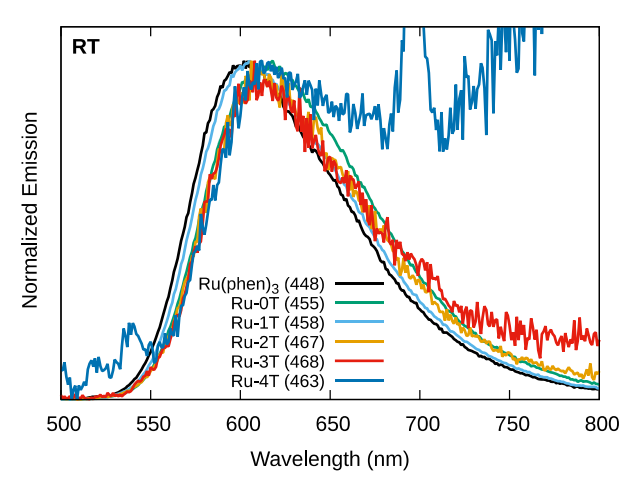
Figure 7: UV-vis spectra of [Ru(phen)₃]²⁺ and the **Ru-nT** series as PF₆⁻ salts in MeCN.

The electronic absorption spectra of the series collected on the hexafluorophosphate salts in MeCN are shown in Figure 7, and the corresponding molar extinction coefficients are listed in Table 2. $[Ru(phen)_3]^{2+}$ has been previously reported, and our data are in agreement with published values. The spectra can be generalized by two distinct regions. The sharper peaks below 300 nm, with maxima around 223 and 263 nm, are similar across the series and can be ascribed to $\pi \rightarrow \pi^*$ transitions involving the phen coligands and possibly the phen portion of the IP/IP-nT ligands that are proximal to the metal center. These peaks occur at the same energy in related complexes and are not significantly affected by the length of the pendant nT chain.

Table 2: Molar Extinction Coefficients at Various Absorption Peak Maxima for the Ru-nT series.

Compound	λ_{abs} (nm) (log (ϵ / M ⁻¹ cm ⁻¹))
[Ru(phen) ₃] ²⁺	444 (4.20), 263 (4.91), 221 (4.84)
Ru-0T	450 (4.46), 263 (5.17), 223 (5.09)
Ru-1T	457 (4.49), 332 (4.56), 289 (4.95), 264 (5.15), 223 (5.08)
Ru-2T	457 (4.44), 384 (4.69), 263 (5.08), 223 (4.97)
Ru-3T	460 (4.57), 413 (4.75), 263 (5.05), 222 (4.94)
Ru-4T	465 (4.75), 436 (4.84), 264 (5.03), 223 (4.93)

At wavelengths between 300 to 500 nm, the absorption spectra for $[Ru(phen)_3]^{2+}$ and Ru-0T are similar and typical of Ru(II) polypyridyl type complexes with $Ru^{2+}(d\pi) \rightarrow LL(\pi^*)$ MLCT transitions involving phen or phen/IP, respectively, as the π^* acceptor orbitals. The complexes with IP-nT ligands have additional contributions from 1LLCT ($nT\rightarrow IP$) transitions as well as 1ILCT ($nT\rightarrow nT$) for Ru-2T to Ru-4T. These isolated transitions can be seen in the absorption spectra of the analogous uncomplexed IP-nT ligands and free oligothiophenes 128 but do experience some shifting when incorporated into the metal complexes. Our computational studies considering the occupied and virtual NTOs of the Ru-nT complexes highlight the predominant configurations of the computed absorption transitions occurring >400 nm and support these ligand-based contributions. The lowest energy singlet-singlet transitions were computed to be mixed $^1MLCT/^1LLCT$ for Ru-2T and $^1ILCT/^1LLCT$ for Ru-3T and Ru-4T (Figure 5 and Figure S24, Table S4). These computed and experimental energies were lowest for Ru-4T, as expected for the more extended π system, and the 1ILCT character was almost two-fold higher (Figure 5).



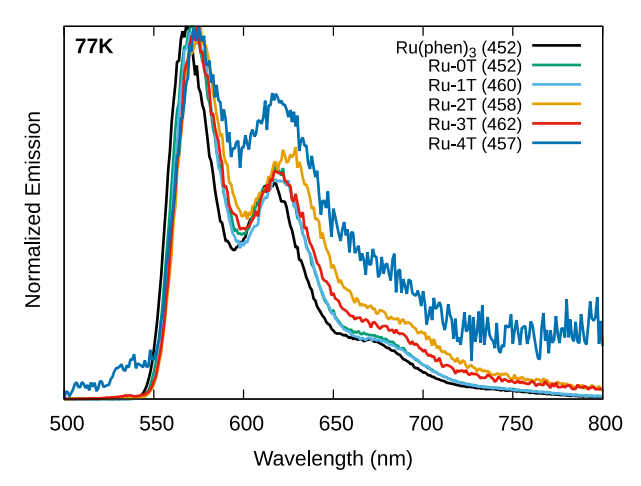


Figure 8: Normalized emission spectra of $[Ru(phen)_3]^{2+}$ and the **Ru-nT** series as PF₆⁻ salts at room temperature (left) and at 77 K (right) in MeCN. The room temperature spectra used argon-sparged MeCN and the 77 K spectra used a 4:1 EtOH:MeOH glass. The excitation wavelengths are noted in parentheses. Emission from **Ru-4T** was weak and superimposed on scatter in the room temperature measurement (blue curves).

All of the complexes in the series exhibited red emission near 610–620 nm as a single, broad and featureless band in argon-sparged MeCN at room temperature (Figure 8, Table 3 and S5). The number of appended thiophene rings did not affect the emission energies, suggesting that the luminescence originates from a common ³MLCT state with similar ligand acceptor orbitals across the series. The computed adiabatic ³MLCT energies matched the experimental room temperature ³MLCT emission energies at around 2.2 eV. For complexes lacking thienyl groups and **Ru-1T**, this ³MLCT state was computed as the lowest-energy triplet state (T₁). For **Ru-2T** to **Ru-4T**, the emissive ³MLCT state was T₂.

The room temperature emission for $[Ru(phen)_3]^{2+}$ was in agreement with that previously reported, ^{129,130} with a quantum yield near 3% and lifetime of approximately 0.5 µs at room temperature. The rest of the complexes in the series also had emission lifetimes between 0.5 and ~1 µs (Table 3 and Figure S27), but quantum yields dropped progressively on going from **Ru-0T** to **Ru-4T**. For complexes with up to two thiophene rings, quantum yields were still between 3 and 8.5%. However, emission from complexes with longer thiophene chains was considerably weaker, falling to about 0.4% for **Ru-3T** and only 0.02% for **Ru-4T**. The spectra in Figure 8 are normalized to emphasize similar ³MLCT emission energies, but the much lower quantum yields for **Ru-3T** and **Ru-4T** are reflected in the poorer signal-to-noise ratios evident in the spectra. The emission from **Ru-4T** is extremely weak and should be regarded as almost non-emissive with an extremely high error on the quantum yield as a result.

Assignment of the emission to 3 MLCT states was corroborated by measurements at 77 K, where the emission shifted to shorter wavelengths with increased quantum yields and exhibited vibronic character typical of 3 MLCT states (Figure 8). The vibronic intervals of around 1350 cm⁻¹ are consistent with diimine involvement in the emissive state, 131 and did not vary significantly throughout the series. The thermally induced Stokes shifts ($\Delta E_{\rm S}$) of around 1100 cm⁻¹ compare well to the related model complex [Ru(bpy)₃]²⁺ ($\Delta E_{\rm S}$ = 1127 cm⁻¹). These 3 MLCT emission energies were computed at around 2.0 eV, in agreement with the experimental 77 K energies (Table 3 and Table S5).

4.3.2 Singlet oxygen sensitization

All of the complexes have triplet excited states of sufficient energy to sensitize ${}^{1}O_{2}$ with an energy of approximately 0.97 eV. 133 The quantum yields for ${}^{1}O_{2}$ formation (Φ_{Δ}) were calculated for the PF₆⁻ salts in

air-saturated MeCN calculated using the integrated ${}^{1}O_{2}$ emission centered near 1276 nm with $[Ru(bpy)_{3}](PF_{6})_{2}$ as the standard $(\Phi_{\Delta,s}=0.56)$ according to Equation 1.¹³³ The results are compiled in Table 3. The ${}^{1}O_{2}$ quantum yields for $Ru(phen)_{3}^{2+}$ and Ru-0T, the compounds lacking any thiophene rings, were very similar to the reference at 53 and 56%, respectively. Generation of ${}^{1}O_{2}$ increased with thienyl chain length, plateauing around 88% at n=3. For comparison, the related complexes $[Ru(bpy)_{2}(IP-nT)]^{2+}$ and [Ru(4,4'-dmb) $_{2}(IP-nT)]^{2+}$ exhibit near unity quantum yields for n=3,4 and around 75% for n=2.⁹⁸

Table 3: Photophysical properties of the series, measured as $(PF_6)^-$ salts in MeCN. Excitation wavelengths are noted in parentheses. *Too weak to accurately quantify.

Compound	RT em			77 K emission		$\Phi_{\!\scriptscriptstyle \Delta}$	- /
Compound	$\lambda_{\text{em.}}$ (λ_{ex}) / nm	Φ_{em}	τ _{em} / μs	$\lambda_{\text{em.}} \left(\lambda_{\text{ex}} \right) / \text{ nm}$	Ф _{ет,77 К}	(λ _{ex} / nm)	τ _{TA} / μs
[Ru(phen) ₃] ²⁺	602 (448)	3.1×10 ⁻²	0.47	568, 616, 672 (452)	5.5×10 ⁻¹	0.53 (450)	0.40
Ru-0T	617 (455)	8.4×10 ⁻²	0.70	571, 620, 679 (452)	5.6×10 ⁻¹	0.56 (456)	0.85
Ru-1T	606 (458)	5.7×10 ⁻²	0.73	573, 621, 678 (460)	4.4×10 ⁻¹	0.62 (461)	0.18, 0.79 (410, 460) 0.16 (610)
Ru-2T	612 (467)	3.0×10 ⁻²	1.1	576, 625, 692 (458)	3.2×10 ⁻²	0.73 (462)	148
Ru-3T	614 (468)	3.5×10 ⁻³	0.97	573, 620, 685 (462)	1.7×10 ⁻²	0.88 (457)	34–36
Ru-4T	614 (463)	*1.6×10 ⁻⁴	0.85	574, 619 (457)	8.6×10 ⁻⁴	0.87 (462)	25

4.3.3 Transient Absorption

Nanosecond transient absorption (TA) spectroscopy was used to examine the triplet excited states. Differential excited state absorption (ESA) spectra were measured in degassed MeCN following excitation with a 355 nm laser with a 5-ns pulse width, with correction for luminescence. Selected time slices are shown in Figure 9 and the full set of TA spectra are compiled in Figure S28. Transient lifetimes were measured at ESA maxima or bleach minima and are compiled in Table 3. The corresponding time-resolved spectra and fits are shown in Figure S29.

The TA profiles of $[Ru(phen)_3]^{2+}$ and **Ru-0T** are typical of what might be expected of the 3MLCT state for a Ru(II) polypyridyl complex, with a bleach in the 400 to 500 nm region arising from loss of the strong ${}^1MLCT \leftarrow {}^1A_1$ ground state absorption. Part of the ESA due to the ligand phen⁻ transitions can be seen at shorter wavelengths, and the extremely weak and broad absorption at longer wavelengths due to phen⁻ or LMCT transitions involving Ru(II) is also observed. Their TA lifetimes matched their emissive lifetimes and lacked any involvement of the higher-lying ligand-based triplet excited states.

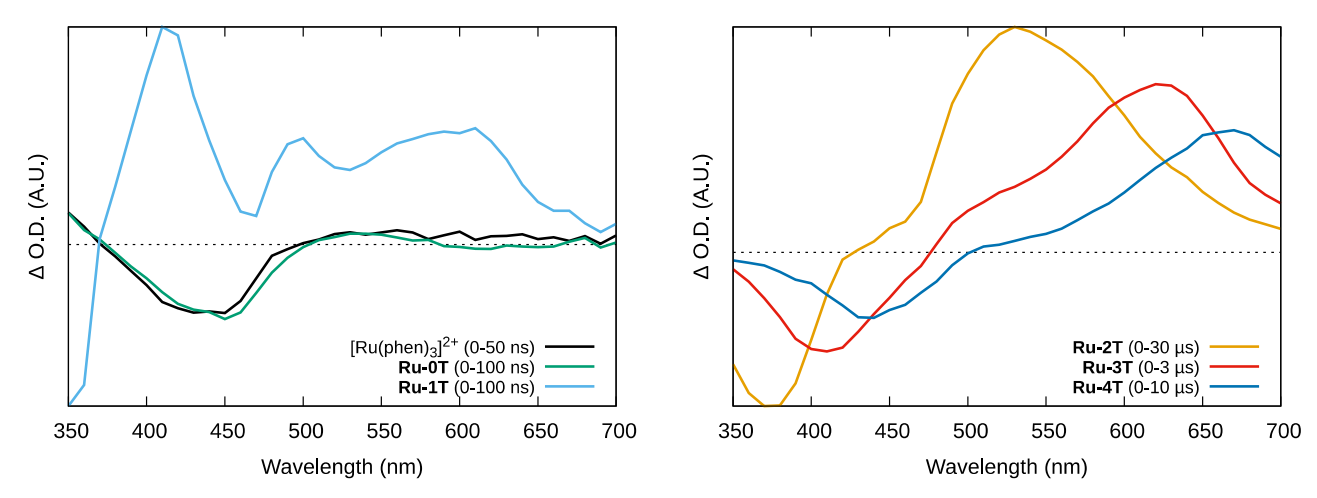


Figure 9: Transient absorption (TA) spectra of $[Ru(phen)_3]^{2+}$ and the **Ru-nT** series in deoxygenated MeCN integrated over the indicated time slice following the excitation pulse. $\Delta O.D.=0$ is indicated by a dotted line. Data for the complexes with nanosecond lifetimes are shown on the left, and those with microsecond lifetimes are shown on the right.

The transient profile of **Ru-1T** is more complex. A strong ground state bleach appears near 350 nm alongside a strong ESA near 410 nm that overlaps the weaker 1 MLCT \leftarrow 1 A₁ ground state bleach in the 400 to 500 nm region and another ESA beyond 475 nm (Figure 9 and **Figure S28**). The ESA at longer wavelengths is more intense than that for [Ru(phen)₃]²⁺ or **Ru-0T** but not nearly as strong as typical 3 ILCT states involving two or more thiophenes. The kinetics measured at 410 and 460 nm both exhibited a fast decay (0.2 µs) of the ESA component and a slower decay (0.8 µs) of a bleach component. The slower decay was in good agreement with the 3 MLCT decay from the emission experiment, and the TA spectrum collected at 0.5–1.0 µs after the laser pulse exhibits the typical 3 MLCT signature (Figure S30). The ESA at longer wavelengths (e.g., 610 nm) decayed with a single time constant of 0.2 µs. The strong overlap between the IP-1T ligand-localized absorption and the excitation laser pulse (355 nm) may give rise to the short decay associated with the broad ESA.

Ru-2T has the longest triplet lifetime of the family, and its TA spectrum is dominated by IP-2T ligand-localized transitions. An intense ESA, with an onset near 450 nm and characteristic signature of the oligothiophene-based 3 ILCT state, obscured the 1 MLCT ground state bleach in the 400-500 nm region. The intense bleach in the region under 400 nm, with a minimum near 380 nm, involves the loss of the 1 IL/ 1 ILCT ground state absorption. The decay kinetics in both the bleach and ESA regions are monoexponential with a lifetime of 148 μ s.

The TA spectra of **Ru-3T** and **Ru-4T** are also dominated by the oligothiophene-based ³ILCT triplets. **Ru-3T** exhibited a bleach around 410 nm and a strong ESA near 625 nm, while **Ru-4T** produced these corresponding transients at slightly longer wavelengths. The bleach for **Ru-4T** has its minimum around 440 nm, and the ESA is centered around 675 nm. Both the bleach and the ESA for both compounds decayed monoexponentially with a lifetime of 36 µs for **Ru-3T** and 25 µs for **Ru-4T**. The ³ILCT state that was observed by TA and the emitting ³MLCT state were decoupled as observed in the case of **Ru-2T**, suggesting that the ³ILCT state is the lowest-energy triplet for *n*=2–4. Indeed, the computational studies estimate T₁ as predominantly ³ILCT/³LLCT for **Ru-2T** and ³ILCT for **Ru-3T** and **Ru-4T** (Table 1). The systematic decrease in the ³ILCT state lifetime on going from **Ru-2T** to **Ru-4T**, with T_{TA} dropping from 148 to 36 to 25 µs, is consistent with the shortening of triplet lifetimes in free oligothiophenes owing to the

decrease in the T_1 – S_0 energy gap with increasing number of thiophenes. ¹²⁸ The absence of ³MLCT contributions to the decays is consistent with the extremely weak ³MLCT emission quantum yields that suggest the ³ILCT state dominates the relaxation dynamics on the nanosecond to microsecond timescales.

4.3.4 Triplet Energies and Excited State Pathways

The energies of the oligothiophene-based ³ILCT states cannot be obtained directly because these states are non-emissive, nor can they be estimated from the corresponding free IP-*n*T ligands and *n*T units because they also do not emit. However, the ³ILCT energies can be estimated based on the shortening of their TA lifetimes in the presence of suitable excited state quenchers, in accordance with the modified Stern-Volmer relationship presented in Equation S 2. The complexes were excited at 532 nm to avoid directly exciting the quencher. The appearance of a new long-lived signal in the ESA spectra of the mixtures confirmed that the triplet state of the quencher had indeed formed via energy transfer from the excited complex.

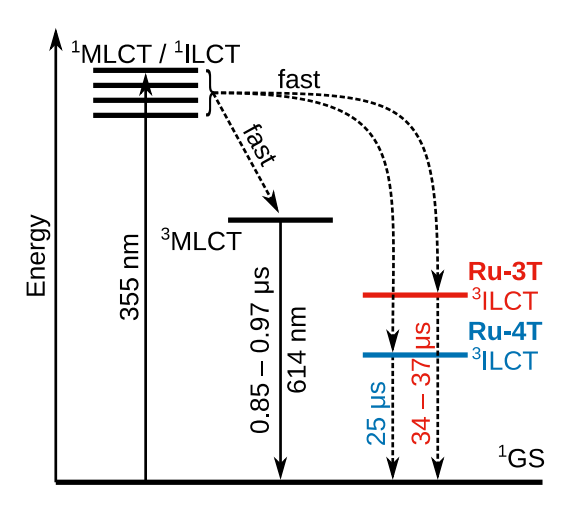
The rate constants (k_q) for triplet-triplet energy transfer between selected organic sensitizers of known ${}^3\pi\pi^*$ energies 67,134 (E_T) and the excited complexes are compiled in Table 4. Values for k_q were determined by examining the TA lifetimes of the complexes (measured at 620 nm and at 660 nm for **Ru-3T** and **Ru-4T**, respectively) as a function of quencher concentration. The values for k_q were largest when the ${}^3\pi\pi^*$ acceptor energy was near 1.53 eV. Therefore, the 3 ILCT energies were estimated to lie near 1.5 eV above the ground state. These values are in good agreement with the computed 3 ILCT energies of 1.57 for **Ru-3T** and 1.44 eV for **Ru-4T**.

Table 4: Stern-Volmer triplet-triplet energy transfer rate constants for **Ru-3T** and **Ru-4T** in the presence of quenchers with known $^3\pi\pi^*$ energies (E_T). n.d.=not determined.

Quencher	E ₇ (eV)	Ru-3T k_q (M ⁻¹ s ⁻¹)	Ru-4T k_q (M ⁻¹ s ⁻¹)
tetracene	1.27	9.4 × 10 ⁸	n.d.
perylene	1.53	5.2 × 10 ⁹	3.7×10^9
diBr-anthracene	1.74	2.9 × 10 ⁹	6.2 × 10 ⁸
phenazine	1.93	1.2 × 10 ⁸	3.1 × 10 ⁸
pyrene	2.10	2.3×10^7	n.d.
fluorene	2.92	0	n.d.

From the spectroscopic data combined with computational studies and Stern-Volmer quenching experiments, Jablonski diagrams modelling the excited state pathways for the two complexes with predominant ³ILCT states are shown in Scheme 1. Excitation of **Ru-3T** and **Ru-4T** with visible light produces singlet excited states of mixed ¹MLCT, ¹LLCT, or ¹ILCT configurations, where the computed singlet-singlet transitions have higher ¹ILCT character for the longest wavelength absorption bands (Table S3). For example, **Ru-3T** has 58% ³ILCT character for its 466 nm transition and **Ru-4T** has 77% for its 488 nm transition. These initially formed excited states ultimately relax to their lower-lying triplets of ³MLCT (T₂) or ³ILCT (T₁) configuration where T₁ has a small amount of ³LLCT mixing (27% for **Ru-3T** and 19% for **Ru-4T**). The ³MLCT emission is weak, and the excited state dynamics of **Ru-3T** and **Ru-4T** on the nanosecond to microsecond timescales in the TA experiments are dominated by lowest-lying ³ILCT states with longer lifetimes (25–40 µs). These dynamics are similar to those we have encountered previously in other oligothienyl-containing complexes.^{23,24,99,135–139} While both ³MLCT and ³ILCT states can generate ¹O₂, it is expected that the ³ILCT states with their longer lifetimes may play the larger role in ROS production. Because oligothiophenes are known to be redox active, these states may also be

deactivated via electron transfer pathways in the presence of suitable electron donors or acceptors. The electrochemical properties of **Ru-3T** and **Ru-4T** along with the rest of the series were investigated to gain a better understanding of these characteristics.



Scheme 1: Jablonksi diagram depicting the excited state pathways of **Ru-3T** and **Ru-4T**. Energies are not to scale and ¹LLCT contribution to initially formed excited states not shown.

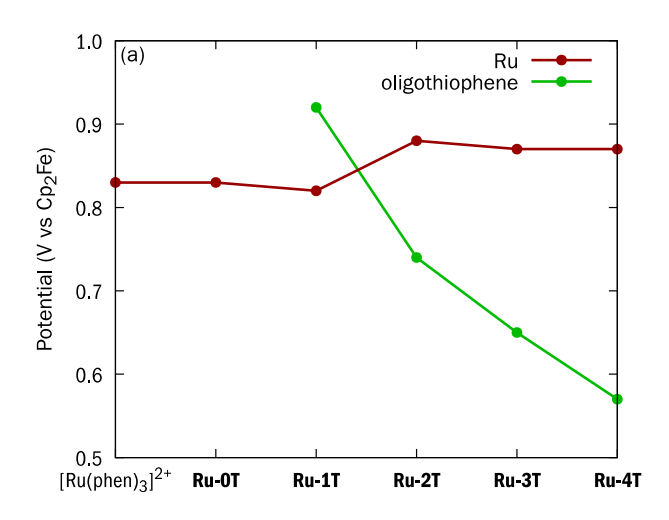
4.4 Electrochemistry

4.4.1 Oxidation of [Ru(phen)₂(IP-nT)](PF₆)₂ complexes

Representative cyclic differential pulse voltammetry (CDPV) traces for oxidation of the complexes measured relative to Ag/AgCl (4M KCl) are presented in Figure S31, and the formal redox potentials are listed in Table 5 relative to ferrocene as the internal standard. The trends are compared in Figure 10. As is typical of Ru(II) polypyridyl complexes, a single reversible wave appears due to the Ru²⁺/ Ru³⁺ process, occurring near +820 to +880 mV vs. ferrocene in all the complexes. The potential for the Ru²⁺/ Ru³⁺ couple is largely unaffected by the length of the thienyl chain. For compounds **Ru-1T** through **Ru-4T**, a second, quasi-reversible wave appears, due to the oxidation of the thiophene chain. For two thienyl groups and longer, nT is more easily oxidized than the Ru(II) center. In contrast, the thiophene oxidation is less favorable than the metal oxidation by about 100 mV for **Ru-1T**. The change with each successive thiophene group is most pronounced on going from one to two thiophenes, with a difference of about 180 mV. Thereafter, the changes are around 80 to 90 mV. The difference in the nT oxidation potentials of **Ru-4T** versus **Ru-1T** is about 350 mV. This trend is consistent with the behaviour of free oligothiophenes, with oxidation occurring more readily for longer nT.¹⁴⁰

4.4.2 Reduction of [Ru(phen)₂(IP-nT)](PF₆)₂ complexes

The electrochemistry of Ru(II) polypyridyl complexes of this type is generally typified by three reversible reduction waves as one electron is added to each ligand in succession. The reduction of [Ru(phen)3]²⁺ is known to be complicated by adsorption on the electrode, the found this problem could be mitigated using DMF as the solvent and a lower concentration (0.25 mM) on the reduction sweep.



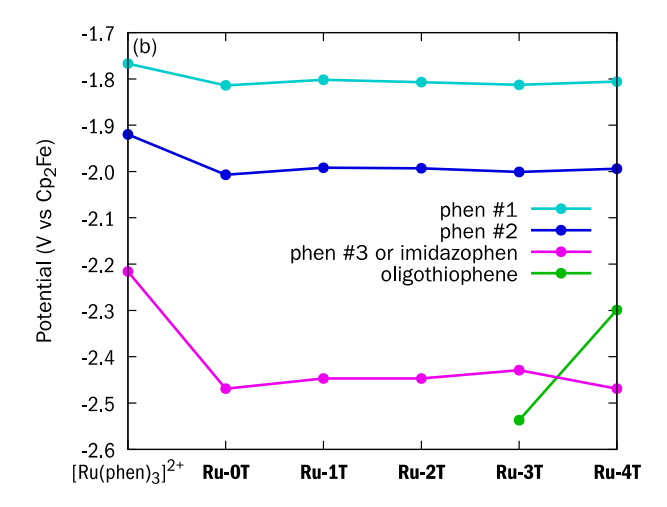


Figure 10: Formal redox potentials (vs the ferrocene internal reference) and proposed assignments of the (a) oxidation and (b) reduction processes, as measured by CDPV in DMF containing TBAPF₆.

The cyclic voltammograms are shown in Figure S32 and the formal potentials are tabulated in Table 5 and compared graphically in Figure 10. The first two reduction waves for the \mathbf{Ru} - $n\mathbf{T}$ series shift to slightly more negative potentials compared to the model compound $[\mathrm{Ru}(\mathrm{phen})_3]^{2+}$. In contrast, the potential of third reduction changes more dramatically, shifting negative by around 250 mV, when phen is replaced by IP but is also largely unaffected by n. This indicates that the first two reductions involve the phen ligands, and the third reduction involves the IP- $n\mathbf{T}$ ligand.

The potential of the third reduction of the **Ru-nT** complexes does not change much, becoming more positive by only around 40 mV on going from **Ru-0T** to **Ru-3T**. This suggests that the reduction is localized to the IP portion of the IP-nT ligand and is influenced only slightly by the number of thiophenes. A fourth reduction appears only in the case of **Ru-3T** and **Ru-4T**. This fourth reduction potential shifts positive by 240 mV on going from **Ru-3T** to **Ru-4T**, in agreement with smaller HOMO-LUMO gaps associated with increasing π -conjugation in oligothiophenes. ¹⁴² Although **Ru-3T** is the first complex in the series where the oligothiophene unit can be reduced in the measurable potential window, 3T remains harder to reduce than IP. **Ru-4T** shows a marked departure and represents the first point at which the oligothiophene unit is reduced more readily than IP (Figure 10b).

Table 5. Formal redox potentials measured by CDPV in DMF containing 0.1 M TBAPF $_6$, referenced in volts against ferrocene as the internal standard. The concentration of the complexes was 4 mM for the oxidation and 0.25 mM for the reduction scans. The working and reference electrodes were glassy carbon and Ag/AgCl/4M KCl, respectively. Overlapping waves were deconvoluted mathematically. The error on these measurements is ± 0.02 V.

Compound	$E_{red}^{0'}(4)$	$E_{red}^{0'}(3)$	$E_{red}^{0'}(2)$	$E_{red}^{0'}(1)$	$E_{ox}^{0'}(1)$	$E_{ox}^{0'}(2)$
[Ru(phen) ₃] ²⁺		-2.22	-1.92	-1.78	+0.83	
Ru-0T		-2.46	-2.00	-1.81	+0.83	
Ru-1T		-2.45	-1.99	-1.81	+0.82	+0.92 ^{b,c}
Ru-2T		-2.45	-1.99	-1.81	+0.74 ^{b,c}	+0.88
Ru-3T	-2.53a	-2.44	-1.99	-1.81	+0.65 ^{b,c}	+0.87
Ru-4T	-2.47	-2.30 ^a	-1.99	-1.81	+0.57 ^{b,c}	+0.87

^areduction of oligothiophene unit. ^bquasi-reversible. ^coxidation of oligothiophene unit.

4.4.3 Excited state redox potentials

The excited state redox potentials of Ru(II) polypyridyl complexes have been approximated from the ground state oxidation and reduction potentials and E_{00} , the energy difference between the thermally equilibrated excited state and the ground state zeroth vibrational level.¹⁴³ These earlier studies use the 77 K emission to estimate E_{00} . In the present series, the capacities of the oligothiophene units of **Ru-3T** and **Ru-4T** to also be oxidized and reduced in the ground state prompted us to estimate the redox power of the 3 ILCT state in addition to the 3 MLCT state (Table 6). Since the long-lived 3 ILCT state is non-emissive in this series, its computed energy from Table S5 was used. The E_{00} of the 3 MLCT is taken from the most intense emission peak energy as measured in a 4:1 ethanol:methanol glass at 77 K. The potentials for oxidation (Equation 1) and reduction (Equation 2) of the excited states were estimated from simple thermodynamic considerations, where 3 PS* denotes the 3 MLCT or longer-lived 3 ILCT state. 129,143

$$E(^{3}PS^{*} \leftarrow PS^{+} + e^{-}) = E(PS \leftarrow PS^{+} + e^{-}) - E_{00}$$
 Equation 1
 $E(^{3}PS^{*} + e^{-} \rightarrow PS^{-}) = E(PS + e^{-} \rightarrow PS^{-}) + E_{00}$ Equation 2

The ground state redox potentials related to the ³MLCT state correspond to the Ru^{3+/2+} oxidation and the first phen^{0/-} reduction voltametric waves and are similar throughout the series. This is consistent with an ³MLCT excited state that involves ligands proximal to the Ru(II) center and thus largely unaffected by the presence and number of thiophenes. For all compounds, the Ru^{3+/2+} oxidation potentials in the excited state were near –1.29 V and the first phen^{0/-} reduction potentials in the excited state were around 0.35 V.

Since the 3 ILCT state involves the nT unit, 23,63 the waves corresponding to oligothiophene oxidation and reduction were used to estimate E^*_{ox} and E^*_{red} , respectively. E^*_{red} was also estimated using the IP reduction since T₁ has a small amount of 3 LLCT character. These values were estimated for **Ru-3T** and **Ru-4T**, the only two compounds in the series that showed both oxidations and reductions involving the IP-nT ligand and for which T₁ was predominantly 3 ILCT.

Although the nT unit is more easily oxidized compared to the Ru(II) center in the ground state (Figure 10), the Ru(II) center is the better reducing species in the ${}^{3}MLCT$ excited state (-1.29 V versus -0.92 for **Ru-3T** and -0.87 for **Ru-4T**). The reason for this difference is due to the higher energy stored in the ${}^{3}MLCT$ state compared to the ${}^{3}ILCT$ states (2.16 eV versus 1.57 for **Ru-3T** and 1.44 for **Ru-4T**) that offsets the differences in reducing power of the ground states. The phen ligand is the most easily reduced ligand in both the ground and the excited states, resulting in the ${}^{3}MLCT$ state being much more oxidizing than the ${}^{3}ILCT$ state (0.35 V versus -0.96 for **Ru-3T** or -0.86 for **Ru-4T**). Nevertheless, any excited state redox processes contributing to photocytotoxicity could involve the ${}^{3}ILCT$ state given that it may be formed in much higher yield and with a lifetime that is 30 to 40×100 longer.

Table 6: Excited state redox potentials for the 3 MLCT and 3 ILCT states of **Ru-3T** and **Ru-4T**, vs. ferrocene in DMF. E^{*}_{red} for the 3 ILCT state was estimated two ways: using $E^{0'}_{red}$ involving nT or IP. The latter number is in parentheses.

	³ MLCT			3ILCT		
Complex	<i>E</i> ₀₀ (eV)	E*₀x (V vs. Cp₂Fe)	E* _{red} (V vs. Cp ₂ Fe)	<i>E</i> ₀₀ (eV)	E* _{ox} (V vs. Cp₂Fe)	E* _{red} (V vs. Cp ₂ Fe)
Ru-3T	2.16	-1.29	0.35	1.57	-0.92	-0.96 (-0.87)
Ru-4T	2.16	-1.29	0.35	1.44	-0.87	-0.86 (-1.03)

4.5 Photobiological activity

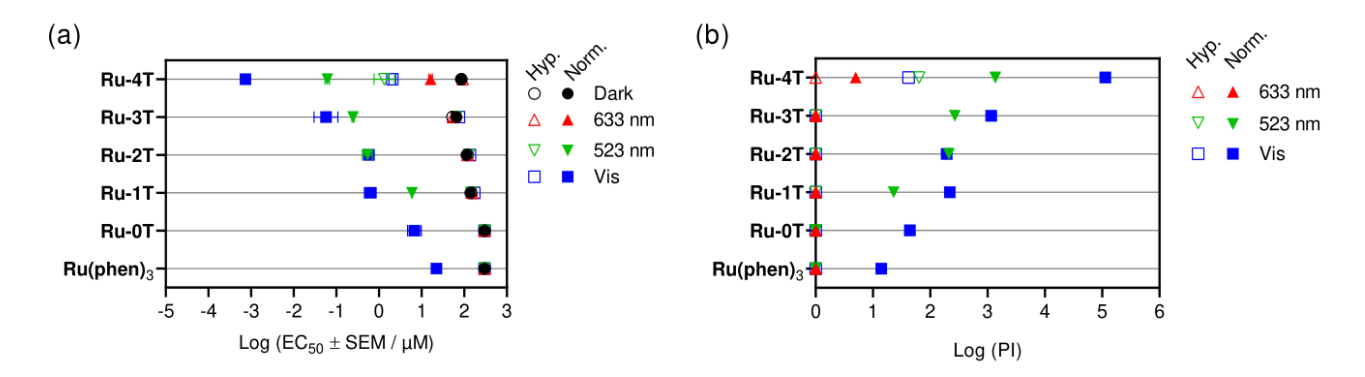


Figure 11: Summary of in vitro cytotoxicity and photocytotoxicity reported as log (EC₅₀ \pm SEM) values (a) and PI values (b) obtained from dose–response curves in the SK-MEL-28 melanoma cell line with [Ru(phen)₃](CI)₂ and **Ru-0T-Ru-4T**. Treatments included dark (0 J cm⁻²; black circles) and 100 J cm⁻² doses of 633 nm (red triangles), 523 nm (green inverted triangles), and visible (400–700 nm) light (blue squares) light. The irradiance was approximately 20 mW cm⁻¹. Hypoxic (1% O₂) results are shown with open symbols, and normoxic (~18.5% O₂) data are shown with closed symbols.

The complexes in this series were evaluated for their dark and light-triggered cytotoxicities against human skin melanoma cells (SK-MEL-28) cultured as 2D monolayers under normoxic (~18.5% O₂) and hypoxic (~1% O₂) conditions (Figure 11). Details can be found in our previously published procedures⁶³ and also in the SI. Stock solutions of [Ru(phen)₃](Cl)₂ and **Ru-0T-Ru-3T** were prepared at 5 mM in water containing 10% DMSO with solubilization first in DMSO followed by addition of water. **Ru-4T** was prepared in 100% DMSO.

4.5.1 Normoxia.

Briefly, melanoma cells growing in log phase were seeded into two sets of 384-well plates: one set for cytotoxicity (dark plates) and one set for photocytotoxicity (light plates) evaluation. Cells were allowed to adhere to the wells at 37 °C over a period of 3–5 hours and then treated with varying concentrations of PS (1 nM to 300 μ M for all compounds, 1 aM to 300 μ M for **Ru-4T**) serially diluted in DPBS. Following a 13–20 h drug-to-light-interval (DLI), the light plates were irradiated while the dark plates were kept in the incubator. The light treatment used LEDs emitting broadband visible (400–700 nm, 21 mW cm⁻²) or narrower green (523 nm, 18 mW cm⁻²) or red (633 nm, 18 mW cm⁻²) light with a fluence of 100 J cm⁻². The spectral outputs of the light sources are given in Figure S33. Both dark and light-treated plates were then incubated at 37 °C for an additional 24 h before assessing cell viability with a resazurin-based assay. The effective concentrations to reduce cell viability by 50% (EC50 values) were calculated from sigmoidal fits of the dose-response curves for the dark and light-treated conditions based on three technical replicates. The phototherapeutic indices (PIs), representing light-triggered amplification of cytotoxic effects, were tabulated as ratios of the dark to light EC50 values.

The complexes of this series were relatively nontoxic to SK-MEL-28 cells in the absence of a light trigger (Figure 11a, Table S6). Only **Ru-3T** and **Ru-4T** had dark EC₅₀ values <100 μ M, which were still considered nontoxic (66.4 and 84.0 μ M, respectively). [Ru(phen)₃](Cl)₂ and **Ru-0T** had dark EC₅₀ values that were beyond the highest concentration tested in the assay and were tabulated as >300 μ M. As a

consequence, their PI values are undefined but reported as a lower limit using 300 μ M as the dark cytotoxicity.

Broad-band visible light produced photocytotoxicity from all compounds in the series (Figure 11, Table S6). Systematic π-expansion from phen to IP-nT (n=1–4 thienyl groups) resulted in progressively higher potency using visible light, spanning four orders of magnitude. The visible light EC₅₀ values in normoxic conditions ranged from 22 μM (PI>10) for the least active reference compound [Ru(phen)₃](CI)₂ to as low as 740 pM (PI>10⁵) for the most active compound **Ru-4T**. Replacing a phen ligand with IP (**Ru-0T**) increased the photocytotoxicity 3-fold (EC₅₀=6.8 μM, PI>40). Appending one (**Ru-1T**) or two (**Ru-2T**) thienyl groups to IP improved the potency another 10-fold, shifting the EC₅₀ values into sub-micromolar regime near 0.6 μM with PIs on order of 200. Another 10-fold enhancement in photocytotoxicity was accomplished on going to three thiophene rings (**Ru-3T**; EC₅₀=0.057 μM, PI~10³), but the greatest change occurred with four thiophenes (**Ru-4T**; EC₅₀=740 pM, PI>10⁵).

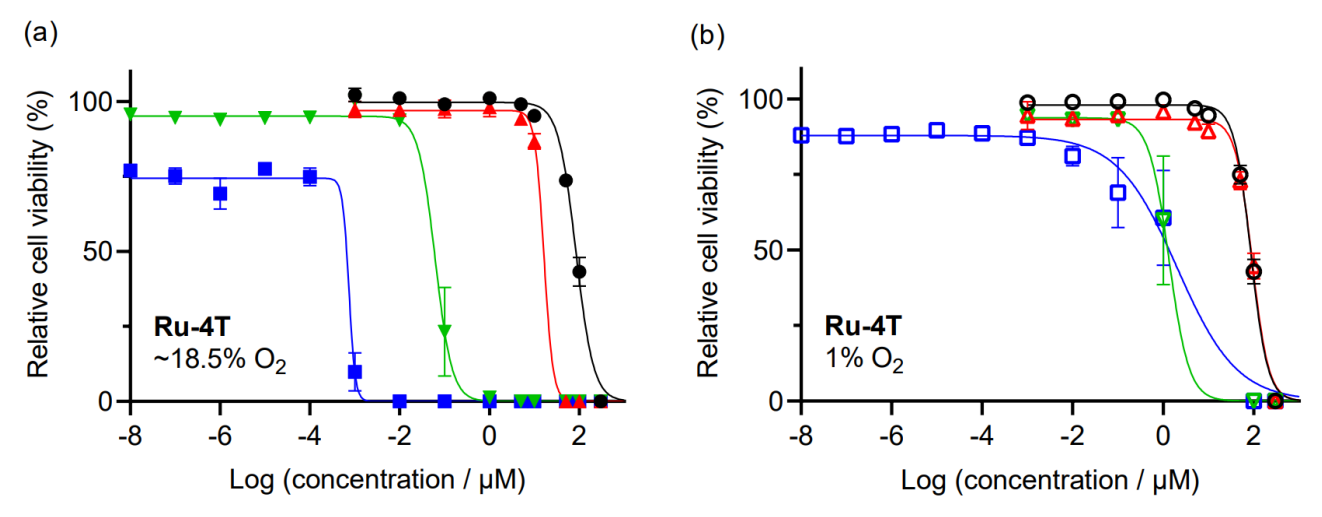


Figure 12. Dose-response (\pm SD) of **Ru-4T** in (a) normoxic \sim 18.5% O₂ or (b) hypoxic 1% O₂-treated SK-MEL-28 melanoma cells. Treatments included dark (0 J cm⁻²; black circles) and 100 J cm⁻² doses of 633 nm (red triangles), 523 nm (green inverted triangles), and visible (400–700 nm, blue squares) light.

All compounds were inactive with red light, with the exception that $\mathbf{Ru\text{-}3T}$ (EC₅₀=16.3 μ M; PI=5) and $\mathbf{Ru\text{-}4T}$ (EC₅₀=16.3 μ M; PI=5) exhibited marginal responses. This is in line with what would be expected for compounds having little absorption of red light.⁶⁹ [Ru(phen)₃](Cl)₂ and $\mathbf{Ru\text{-}0T}$ were also inactive with green light. Therefore, the observed effects with broadband visible light were likely generated preferentially by the shorter wavelengths, which is further supported by the attenuated EC₅₀ values and corresponding PIs for the thienyl-containing complexes with green light. The only exception was $\mathbf{Ru\text{-}2T}$ which maintained its EC₅₀ value near 0.5 μ M and PI of ~200 with green light. The PIs for both $\mathbf{Ru\text{-}1T}$ and $\mathbf{Ru\text{-}3T}$ were reduced ten-fold (PI=23 and 270, respectively), while that for $\mathbf{Ru\text{-}4T}$ was reduced by several orders of magnitude (PI=~10³). The photocytotoxic responses elicited by $\mathbf{Ru\text{-}4T}$ toward SK-MEL-28 cells under both oxygen conditions with the different light parameters are compared in Figure 12.

4.5.2 Hypoxia.

The hypoxia assays were carried out as described for normoxia except that the dark and light plates with adhered cells were moved to a hypoxia chamber (1% O₂) for 2–3 h before compound addition. At the end of the DLI in hypoxia, dissolved oxygen was measured using an immersive optical probe to confirm

hypoxic condition before sealing the light plates with highly transparent, low gas permeable qPCR film. The light plates were illuminated outside of the hypoxia chamber alongside the normoxic plates. The films were then removed, and all plates were incubated under normoxia (37°C, 5% CO_2 , \geq 90% RH) for 20–23 h before cell viability determination.

As observed for the normoxic condition, the compounds were nontoxic to cells in the dark and with red light under hypoxia (Figure 11, Table S6). [Ru(phen)₃](Cl)₂ and **Ru-0T-Ru-3T** lost all of their photocytotoxicity with visible and green light in hypoxia, while **Ru-4T** gave modest activity with a visible EC₅₀ values of approximately 1–2 μ M and PIs on the order of 40–60. This marked reduction in activity for **Ru-4T** and inactivity for the rest of the series suggests that the largest contributor to the normoxic photocytotoxicity for this family likely involves oxygen-dependent photophysical pathways.

4.5.3 Biological replicates.

The data shown in Figure 11 and Table S6 represent our initial results and are the average of technical replicates performed in triplicate on cells of the same batch and identical passage number and have low standard deviation as a result. Biological replicates will have more variation, and thus we validated our results for **Ru-3T** and **Ru-4T** over seven biological replicates run in triplicate (Figure 13 and Table S7–Table S10. Repeat 0 is the data from Figure 11 and Table S6 that was discussed above. Repeats 1–6 represent biological replicates with variations as described previously.⁶³

Both Ru-3T and Ru-4T were completely nontoxic over all biological replicates, with mean EC₅₀ values just under 100 µM in both normoxia and hypoxia and standard error of the mean (SEM) being within ±25 μM for Ru-3T and ±10 μM Ru-4T. The visible EC₅₀ values for Ru-3T in normoxia ranged from about 60 to 80 nM with a mean of 64 nM; the corresponding visible PIs ranged from 1200 to 2500 with a mean of 1600. The EC₅₀ value for **Ru-4T** under the same conditions exhibited a much larger variance, ranging from 40 fM to about 8.6 nM with a mean of 2.2 nM. Nevertheless, five of the seven replicates were within an order of magnitude of each other. Three were between 0.64 and 0.80 nM and two were around 4.8 to 8.6 nM, giving rise to PIs on the order of 10⁴ to 10⁵. Only two of the seven biological replicates for **Ru-4T** were well outside of this range at 40 and 320 fM with unusually large PIs of 108-109. Of note, only the most potent IP-4T complexes under the most potent light condition (visible) in the normoxic condition produce more than several orders of magnitude variation in photocytotoxicity between biological replicates, with EC₅₀ values extending into the ubertoxin range (fM and lower) with visible light.⁶³ In the case of the related analog ML19C01, [Ru(2,9-dmp)₂(IP-4T)](Cl)₂, four of six biological replicates fell in this range and produced PIs as large as 10¹². To date, this behavior has only been observed for certain IP-4T complexes of Ru(II) and (to a lesser degree) of Os(II). Herein, Ru-4T adds one more example that may help us better understand this phenomenon in the future.

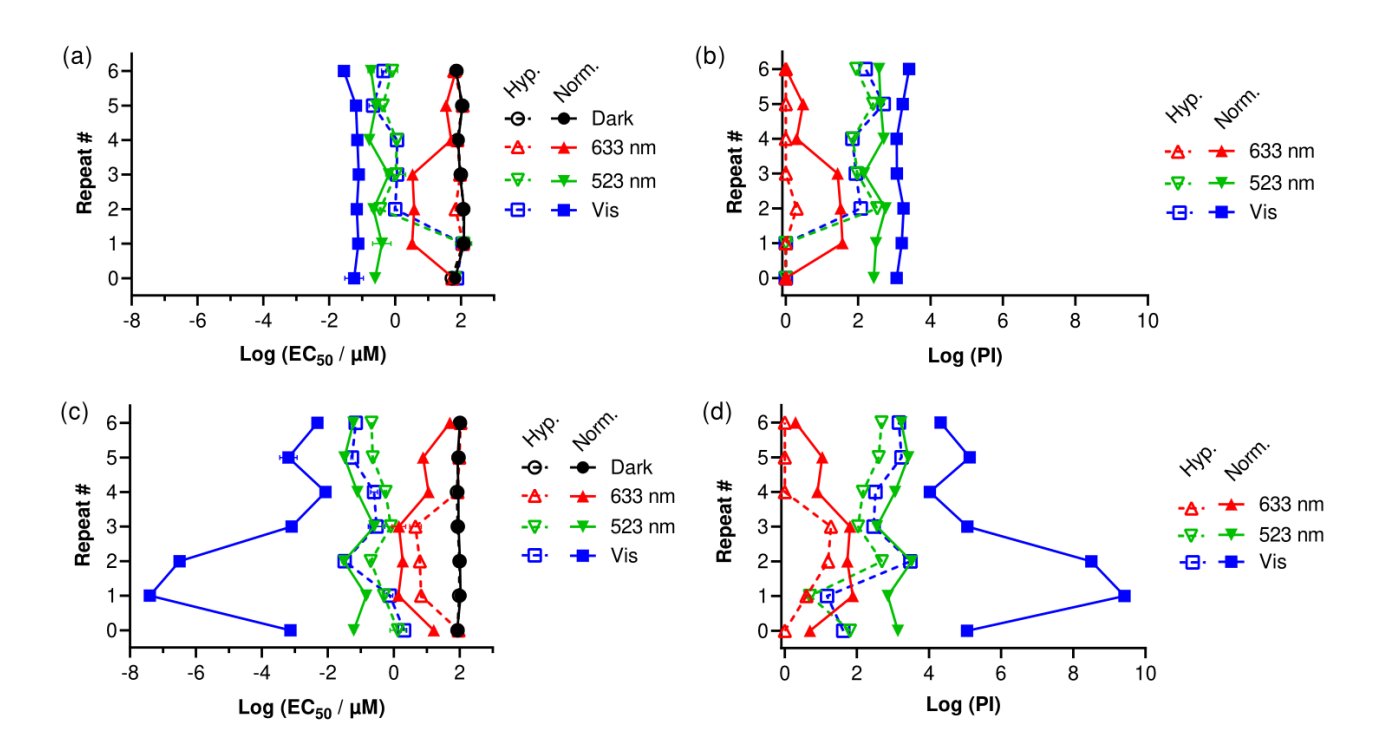


Figure 13. Interassay performance (\pm log(SEM)) of **Ru-3T** (top, a + b) and **Ru-4T** (bottom, c + d) in normoxic (filled symbols, solid lines, ~18.5% O₂) and hypoxic (open symbols, dashed lines, 1% O₂) SK-MEL-28 melanoma cells. Treatments included dark (no light; black circles) and 100 J cm⁻² treatments at ~20 mW cm⁻² of visible (400-700 nm) light (blue square), 523 nm (green inverted triangle) and 633 nm (red triangle). SEM = standard error of the mean.

With green light in normoxia, there was little variance in the activity of Ru-3T. The green EC_{50} values varied from 0.16 to 0.64 μ M and PIs from 140 to 570, with the mean being 0.30 μ M and 370. For Ru-4T, five of seven replicates gave green EC_{50} values between 30 and 80 nM (PIs ranged from 1100 to 3300). The remaining two were between 0.15 and 0.26 μ M (PIs ranged from 360 to 720). On average Ru-4T was more active than Ru-3T but by only about five-fold.

With red light normoxia, **Ru-3T** was inactive in four of seven replicates and only moderately active in the remaining three with red EC₅₀ values around 3 to 4 μ M and PIs around 30 to 40. **Ru-4T** was moderately better, with red EC₅₀ values of 1 to 2 μ M (PIs 64 to 77) in three of the seven replicates but 10 to 50 μ M (PIs 2 to 11) in the remainder.

Despite losing all activity in hypoxia in the initial evaluation, $\mathbf{Ru\text{-}3T}$ was phototoxic with visible and green light in five of the seven biological replicates under hypoxia. Three of the replicates gave EC_{50} values near 1 μ M and two were between 0.22 and 0.45 μ M. The resulting PIs ranged from about 70 to 500. Overall, the activity of $\mathbf{Ru\text{-}3T}$ was reduced by five to fifteen-fold in hypoxia with visible light but only about two-fold for green light (because there was a larger difference in the visible and green EC_{50} values in normoxia). There was no significant activity for $\mathsf{Ru\text{-}3T}$ with red light over seven biological replicates.

Ru-4T was also generally much more active with visible light in hypoxia than the initial evaluation showing single-digit μ M photocytotoxicity. Three of the replicates produced EC₅₀ values between 32 and 70 nM, while two were near 0.25–0.30 μ M. The corresponding PIs were between about 290 and 3000. EC₅₀ values in the two remaining replicates were 2.1 to 6.4 μ M (PIs 15 and 42). The large variance in

photocytotoxicity for **Ru-4T** in normoxia was reduced to only a few orders of magnitude in hypoxia, making the attenuation in activity on going from normoxia to hypoxia much more pronounced for **Ru-4T** compared to **Ru-3T**. Nevertheless, **Ru-4T** was slightly more potent on average than **Ru-3T** in hypoxia.

With green light, the difference between EC $_{50}$ values in normoxia and hypoxia for **Ru-4T** was much less. In five of the seven hypoxic replicates, the green EC $_{50}$ values were between 0.20 and 0.81 μ M (PIs 110 to 480) compared to the mean EC $_{50}$ value of about 0.10 μ M in normoxia (mean PI 1600). With red light, **Ru-4T** was inactive in four of seven replicates and only marginally active in the rest with EC $_{50}$ values between 4 and 20 μ M (PIs between 4 and 20). Again, **Ru-4T** was only slightly more potent on average than **Ru-3T**.

To summarize, Ru-4T is superior to Ru-3T over the seven biological replicates when activated with visible light in normoxia. The light EC_{50} values and corresponding PIs for both compounds are attenuated on going from visible to green to red light, suggesting that the observed effects with broadband visible light are generated primarily by the shorter, bluer wavelengths. The light EC_{50} values and PIs are also attenuated on going from normoxia to 1% hypoxia, with the greatest differences observed with visible light as the most potent condition. For both compounds, the visible light-triggered activity in hypoxia was similar to that with green light in normoxia, and the differences between green light activity in normoxia and hypoxia were relatively small. The compounds were relatively inactive with red light, although Ru-4T did show modest activity in normoxia presumably due to some low probability of directly populating the lowest-lying but spin-forbidden triplet state. Of note, Ru-4T marks another example that follows our recently published ML19C01, with evidence of phototoxic effects at concentrations on the order of fM in several of the biological replicates.

5 CONCLUSIONS

The complexes of this family were designed to vary the number of thienyl groups nT attached to the IP ligand in a family of Ru(II) polypyridyl complexes based on 1,10-phenanthroline as the coligand. The motivation is part of a larger initiative to correlate structural variations with photobiological activities across different coordination complex families where we are considering: metal ion, coligands, thienyl-appended ligands, thienyl groups and number of thiophenes, counter ions, ionizable groups and protonation states, and coordination number and geometry. Within the phen family of IP-nT complexes, the extension of the thiophene chain systematically increased the lipophilicity and shifted the (oligo)thienyl-localized $\pi\pi^*$ transitions to lower energy. The electrochemical properties of the complexes were similar and reminiscent of Ru(II) polypyridyl complexes in general with regard to metal oxidation and ligand reduction. However, complexes with at least one thiophene or more exhibited an additional oxidation, involving the thienyl group(s), that occurred more readily than metal oxidation and with increasing n. **Ru-3T** and **Ru-4T** could also be reduced on the thienyl chain, which was the 4^{th} reduction for **Ru-3T** but 3^{rd} for **Ru-4T**.

The MLCT states for the complexes were similar in energy, with 3 MLCT emission in agreement with typical Ru(II) polypyridyl complexes but quantum yields dropping by one to two orders of magnitude for **Ru-3T** and **Ru-4T**, respectively. The reduced phosphorescence was accompanied by an increase in the 1 O₂ quantum yields and access to 3 ILCT states with prolonged lifetimes. The 3 ILCT state was the lowest-lying triplet for **Ru-2T** to **Ru-4T** and decoupled from the 3 MLCT states. T₁ was computed to be of mixed 3 ILCT/ 3 LLCT character for **Ru-2T**, whereas T₁ was predominantly 3 ILCT (>50%) for **Ru-3T** and **Ru-4T**. The 4 C contribution of 3 LLCT to T₁ decreased with increasing n, with 65% 3 ILCT and <20% 3 LLCT character for **Ru-4T**. The triplet lifetime of **Ru-2T** was the longest at 148 μ s and decreased with additional thiophenes as would be expected for a radiationless process governed by the energy gap law.

The ¹O₂ quantum yields were highest for **Ru-3T** and **Ru-4T** at about 88%.

The high ROS production for the complexes with extended thiophene chains resulted in potent phototoxicity in vitro. With visible light activation, $\mathbf{Ru\text{-}3T}$ consistently yielded EC_{50} values between 10 and 100 nM and PIs greater than 10³. Despite having a slightly lower $^1\mathrm{O}_2$ quantum yield and shorter $^3\mathrm{ILCT}$ lifetime, $\mathbf{Ru\text{-}4T}$ was considerably more potent under the same conditions. On average its light EC_{50} values were sub-nanomolar with PIs in the 10^4 to 10^5 range, but the higher variability in activity led to some measurements in the femtomolar regime and PIs as large as 10^9 . This activity was attenuated with longer wavelengths of light and in 1% hypoxia, but notably $\mathbf{Ru\text{-}4T}$ gave reliable sub-micromolar activity in hypoxia with PI values as high as 3,000. The trends for the most potent compounds $\mathbf{Ru\text{-}3T}$ and $\mathbf{Ru\text{-}4T}$ were verified over seven biological replicates performed in triplicate. The fact that $\mathbf{Ru\text{-}3T}$ could be generally classified as a hypoxia-active photosensitizer underscores the importance of biological replicates as this activity was missed in the initial assessment.

From these studies, a lowest-lying 3 ILCT state appears to be key to potent phototoxicity and activity in hypoxia. While the prolonged excited state lifetime of the nT-localized triplet is important, its precise magnitude and 1 O₂ quantum yield are not sole determinants of potency since (i) **Ru-2T** has the longest lifetime but is not the most phototoxic, and (ii) **Ru-3T** and **Ru-4T** have similar 1 O₂ yields but **Ru-4T** is superior (Figure S34). Alternate pathways could involve other ROS and oxygen-independent electron transfer processes. Although the 3 MLCT states were estimated to be more highly oxidizing and reducing compared to the lowest-lying 3 ILCT states, any excited state redox processes contributing to phototoxicity could involve the 3 ILCT state given that it is the lowest energy triplet with a lifetime that is 30 to 4 O× longer and the n T group is redox active. In addition, higher-lying and conformationally distinct 3 ILCT states cannot be excluded and have been implicated in the picosecond dynamics of similar families.

Our study focused on the photophysical drivers of activity and did not consider biological factors such as cellular uptake and localization, subcellular targets, and cell death pathways that may affect cytotoxicity and potentiate phototoxicity. Future studies are aimed at reconciling both photophysical and biological characteristics to explain the unusual potency of certain oligothienyl-based PSs and building structure-activity relationship (SAR) databases for light-responsive transition metal complexes.

6 ASSOCIATED CONTENT

Additional method information and characterization data may be found in the Supplementary Information. This material is available free of charge via the Internet at https://pubs.acs.org.

6.1 Author Information

6.1.1 Corresponding authors

Colin G. Cameron – Department of Chemistry and Biochemistry, The University of Texas at Arlington, Arlington, Texas 76019-0065, United States; orcid.org/0000-0003-0978-0894; Email: colin.cameron@uta.edu

Sherri A. McFarland – Department of Chemistry and Biochemistry, The University of Texas at Arlington, Arlington, Texas 76019-0065, United States; orcid.org/0000-0002-8028-5055; Email: sherri.mcfarland@uta.edu

6.1.2 Authors

Houston D. Cole – Department of Chemistry and Biochemistry, The University of Texas at Arlington, Arlington, Texas 76019-0065, United States

Abbas Vali – Department of Chemistry and Biochemistry, The University of Texas at Arlington, Arlington, Texas 76019-0065, United States

John A. Roque III – Department of Chemistry and Biochemistry, The University of Texas at Arlington, Arlington, Texas 76019-0065, United States; Department of Chemistry and Biochemistry, The University of North Carolina at Greensboro, Greensboro, North Carolina 27402, United States; Present Address: University of North Carolina at Chapel Hill, Chapel Hill, NC, 27599

Ge Shi – Department of Chemistry and Biochemistry, The University of Texas at Arlington, Arlington, Texas 76019-0065, United States

Gurleen Kaur – Department of Chemistry and Biochemistry, The University of Texas at Arlington, Arlington, Texas 76019-0065, United States

Rachel O. Hodges – Department of Chemistry and Biochemistry, The University of North Carolina at Greensboro, Greensboro, North Carolina 27402, United States; Present Address: Wake Forest University School of Medicine, 307 Winston-Salem, NC 27109

Antonio Francés-Monerris – Institut de Ciència Molecular, Universitat de València, 46071 València, Spain

Marta E. Alberto – Dipartimento di Chimica e Tecnologie Chimiche, Università della Calabria, Arcavacata di Rende, 87036 Italy

6.1.3 Notes

S.A.M. has a potential research conflict of interest due to a financial interest with Theralase Technologies, Inc. and PhotoDynamic, Inc. A management plan has been created to preserve objectivity in research in accordance with UTA policy.

6.2 Acknowledgements

The authors would like to thank the National Cancer Institute (NCI) of the National Institutes of Health (NIH) (Award R01CA222227) as well as the National Science Foundation (NSF) (Award 2102459) for support. The content in this work is solely the responsibility of the authors and does not necessarily represent the official views of the National Institutes of Health or National Science Foundation. The authors also thank Dr. Daniel Todd as UNCG's Triad Mass Spectrometry Facility manager and his assistants Jennifer Simpson and Diane Wallace. S.A.M. likewise thanks Dr. Franklin Moy (UNCG) and Dr. Brian Edwards (UTA) for their experimental support and instrument maintenance as NMR facility managers. The authors also thank Susan Monro, Colin Spencer, Ryan DeCoste, Huimin Yin, and Lance Chamberlain for additional synthesis and characterization support for these complexes that was not reported here.

7 REFERENCES

- (1) Sung, H.; Ferlay, J.; Siegel, R. L.; Laversanne, M.; Soerjomataram, I.; Jemal, A.; Bray, F. Global Cancer Statistics 2020: GLOBOCAN Estimates of Incidence and Mortality Worldwide for 36 Cancers in 185 Countries. *CA A Cancer J Clin* **2021**, *71* (3), 209–249. https://doi.org/10.3322/caac.21660.
- (2) Mellman, I.; Coukos, G.; Dranoff, G. Cancer Immunotherapy Comes of Age. *Nature* **2011**, *480* (7378), 480–489. https://doi.org/10.1038/nature10673.

- (3) Marabelle, A.; Tselikas, L.; De Baere, T.; Houot, R. Intratumoral Immunotherapy: Using the Tumor as the Remedy. *Annals of Oncology* **2017**, *28*, xii33–xii43. https://doi.org/10.1093/annonc/mdx683.
- (4) Meric-Bernstam, F.; Larkin, J.; Tabernero, J.; Bonini, C. Enhancing Anti-Tumour Efficacy with Immunotherapy Combinations. *The Lancet* **2021**, *397* (10278), 1010–1022. https://doi.org/10.1016/S0140-6736(20)32598-8.
- (5) Sawyers, C. Targeted Cancer Therapy. *Nature* **2004**, *432* (7015), 294–297. https://doi.org/10.1038/nature03095.
- (6) Min, H.-Y.; Lee, H.-Y. Molecular Targeted Therapy for Anticancer Treatment. *Exp Mol Med* **2022**, *54* (10), 1670–1694. https://doi.org/10.1038/s12276-022-00864-3.
- (7) Monro, S.; Colón, K. L.; Yin, H.; Roque, J.; Konda, P.; Gujar, S.; Thummel, R. P.; Lilge, L.; Cameron, C. G.; McFarland, S. A. Transition Metal Complexes and Photodynamic Therapy from a Tumor-Centered Approach: Challenges, Opportunities, and Highlights from the Development of TLD1433. *Chem. Rev.* **2019**, *119* (2), 797–828. https://doi.org/10.1021/acs.chemrev.8b00211.
- (8) McFarland, S. A.; Mandel, A.; Dumoulin-White, R.; Gasser, G. Metal-Based Photosensitizers for Photodynamic Therapy: The Future of Multimodal Oncology? *Curr. Opin. Chem. Biol.* **2020**, *56*, 23–27. https://doi.org/10.1016/j.cbpa.2019.10.004.
- (9) Busch, T. M. Local Physiological Changes during Photodynamic Therapy. *Lasers Surg. Med.* **2006**, *38* (5), 494–499. https://doi.org/10.1002/lsm.20355.
- (10) Foster, T. H.; Murant, R. S.; Bryant, R. G.; Knox, R. S.; Gibson, S. L.; Hilf, R. Oxygen Consumption and Diffusion Effects in Photodynamic Therapy. *Radiat. Res.* **1991**, *126* (3), 296–303. https://doi.org/10.2307/3577919.
- (11) Howerton, B. S.; Heidary, D. K.; Glazer, E. C. Strained Ruthenium Complexes Are Potent Light-Activated Anticancer Agents. *Journal of the American Chemical Society* **2012**, *134* (20), 8324–8327. https://doi.org/10.1021/ja3009677.
- (12) Havrylyuk, D.; Stevens, K.; Parkin, S.; Glazer, E. C. Toward Optimal Ru(II) Photocages: Balancing Photochemistry, Stability, and Biocompatibility Through Fine Tuning of Steric, Electronic, and Physiochemical Features. *Inorganic Chemistry* **2020**, *59* (2), 1006–1013. https://doi.org/10.1021/acs.inorgchem.9b02065.
- (13) Loftus, L. M.; White, J. K.; Albani, B. A.; Kohler, L.; Kodanko, J. J.; Thummel, R. P.; Dunbar, K. R.; Turro, C. New Ru^{II} Complex for Dual Activity: Photoinduced Ligand Release and ¹O₂ Production. *Chem. Eur. J.* **2016**, *22* (11), 3704–3708. https://doi.org/10.1002/chem.201504800.
- (14) Toupin, N. P.; Nadella, S.; Steinke, S. J.; Turro, C.; Kodanko, J. J. Dual-Action Ru(II) Complexes with Bulky π-Expansive Ligands: Phototoxicity without DNA Intercalation. *Inorganic Chemistry* 2020, *59* (6), 3919–3933. https://doi.org/10.1021/acs.inorgchem.9b03585.
- (15) Sainuddin, T.; Pinto, M.; Yin, H.; Hetu, M.; Colpitts, J.; McFarland, S. A. Strained Ruthenium Metal–Organic Dyads as Photocisplatin Agents with Dual Action. *J. Inorg. Biochem.* **2016**, *158*, 45–54. https://doi.org/10.1016/j.jinorgbio.2016.01.009.
- (16) Lameijer, L. N.; Ernst, D.; Hopkins, S. L.; Meijer, M. S.; Askes, S. H. C.; Le Dévédec, S. E.; Bonnet, S. A Red-Light-Activated Ruthenium-Caged NAMPT Inhibitor Remains Phototoxic in Hypoxic Cancer Cells. *Angew. Chem. Int. Ed.* 2017, *56* (38), 11549–11553. https://doi.org/10.1002/anie.201703890.
- (17) Al-Afyouni, M. H.; Rohrabaugh, T. N.; Al-Afyouni, K. F.; Turro, C. New Ru(II) Photocages Operative with near-IR Light: New Platform for Drug Delivery in the PDT Window. *Chemical Science* **2018**, 9 (32), 6711–6720. https://doi.org/10.1039/C8SC02094A.
- (18) Feng, W.; Gao, C.; Liu, W.; Ren, H.; Wang, C.; Ge, K.; Li, S.; Zhou, G.; Li, H.; Wang, S.; Jia, G.; Li, Z.; Zhang, J. A Novel Anticancer Theranostic Pro-Prodrug Based on Hypoxia and Photo

- Sequential Control. *Chem. Commun.* **2016**, *52* (60), 9434–9437. https://doi.org/10.1039/C6CC02932A.
- (19) Li, M.-D.; Wong, N.-K.; Xiao, J.; Zhu, R.; Wu, L.; Dai, S.-Y.; Chen, F.; Huang, G.; Xu, L.; Bai, X.; Geraskina, M. R.; Winter, A. H.; Chen, X.; Liu, Y.; Fang, W.; Yang, D.; Phillips, D. L. Dynamics of Oxygen-Independent Photocleavage of Blebbistatin as a One-Photon Blue or Two-Photon Near-Infrared Light-Gated Hydroxyl Radical Photocage. *Journal of the American Chemical Society* 2018, 140 (46), 15957–15968. https://doi.org/10.1021/jacs.8b10235.
- (20) van Rixel, V. H. S.; Ramu, V.; Auyeung, A. B.; Beztsinna, N.; Leger, D. Y.; Lameijer, L. N.; Hilt, S. T.; Le Dévédec, S. E.; Yildiz, T.; Betancourt, T.; Gildner, M. B.; Hudnall, T. W.; Sol, V.; Liagre, B.; Kornienko, A.; Bonnet, S. Photo-Uncaging of a Microtubule-Targeted Rigidin Analogue in Hypoxic Cancer Cells and in a Xenograft Mouse Model. *J. Am. Chem. Soc.* **2019**, *141* (46), 18444–18454. https://doi.org/10.1021/jacs.9b07225.
- (21) Roque, J.; Havrylyuk, D.; Barrett, P. C.; Sainuddin, T.; McCain, J.; Colón, K.; Sparks, W. T.; Bradner, E.; Monro, S.; Heidary, D.; Cameron, C. G.; Glazer, E. C.; McFarland, S. A. Strained, Photoejecting Ru(II) Complexes That Are Cytotoxic Under Hypoxic Conditions. *Photochem. Photobiol.* **2020**, *96* (2), 327–339. https://doi.org/10.1111/php.13174.
- (22) Cole, H. D.; Roque, J. A.; Lifshits, L. M.; Hodges, R.; Barrett, P. C.; Havrylyuk, D.; Heidary, D.; Ramasamy, E.; Cameron, C. G.; Glazer, E. C.; McFarland, S. A. Fine-Feature Modifications to Strained Ruthenium Complexes Radically Alter Their Hypoxic Anticancer Activity. *Photochem & Photobiology* **2022**, *98* (1), 73–84. https://doi.org/10.1111/php.13395.
- (23) Roque III, J. A.; Barrett, P. C.; Cole, H. D.; Lifshits, L. M.; Shi, G.; Monro, S.; von Dohlen, D.; Kim, S.; Russo, N.; Deep, G.; Cameron, C. G.; Alberto, M. E.; McFarland, S. A. Breaking the Barrier: An Osmium Photosensitizer with Unprecedented Hypoxic Phototoxicity for Real World Photodynamic Therapy. *Chem. Sci.* **2020**, *11*, 9784–9806. https://doi.org/10.1039/D0SC03008B.
- (24) Roque, J. A.; Barrett, P. C.; Cole, H. D.; Lifshits, L. M.; Bradner, E.; Shi, G.; von Dohlen, D.; Kim, S.; Russo, N.; Deep, G.; Cameron, C. G.; Alberto, M. E.; McFarland, S. A. Os(II) Oligothienyl Complexes as a Hypoxia-Active Photosensitizer Class for Photodynamic Therapy. *Inorg. Chem.* **2020**, *59* (22), 16341–16360. https://doi.org/10.1021/acs.inorgchem.0c02137.
- (25) Lv, Z.; Wei, H.; Li, Q.; Su, X.; Liu, S.; Zhang, K. Y.; Lv, W.; Zhao, Q.; Li, X.; Huang, W. Achieving Efficient Photodynamic Therapy under Both Normoxia and Hypoxia Using Cyclometalated Ru(II) Photosensitizer through Type I Photochemical Process. *Chemical Science* **2018**, *9* (2), 502–512. https://doi.org/10.1039/C7SC03765A.
- (26) Yu, Q.; Huang, T.; Liu, C.; Zhao, M.; Xie, M.; Li, G.; Liu, S.; Huang, W.; Zhao, Q. Oxygen Self-Sufficient NIR-Activatable Liposomes for Tumor Hypoxia Regulation and Photodynamic Therapy. *Chem. Sci.* **2019**, *10* (39), 9091–9098. https://doi.org/10.1039/C9SC03161H.
- (27) Evans, C. L.; Abu-Yousif, A. O.; Park, Y. J.; Klein, O. J.; Celli, J. P.; Rizvi, I.; Zheng, X.; Hasan, T. Killing Hypoxic Cell Populations in a 3D Tumor Model with EtNBS-PDT. *PLoS ONE* **2011**, *6* (8), e23434. https://doi.org/10.1371/journal.pone.0023434.
- (28) Kuang, S.; Wei, F.; Karges, J.; Ke, L.; Xiong, K.; Liao, X.; Gasser, G.; Ji, L.; Chao, H. Photodecaging of a Mitochondria-Localized Iridium(III) Endoperoxide Complex for Two-Photon Photoactivated Therapy under Hypoxia. *J. Am. Chem. Soc.* **2022**, 4091–4101. https://doi.org/10.1021/jacs.1c13137.
- (29) Mazuryk, O.; Janczy-Cempa, E.; Łagosz, J.; Rutkowska-Zbik, D.; Machnicka, A.; Krasowska, A.; Pietrzyk, P.; Stochel, G.; Brindell, M. Relevance of the Electron Transfer Pathway in Photodynamic Activity of Ru(II) Polypyridyl Complexes Containing 4,7-Diphenyl-1,10-Phenanthroline Ligands under Normoxic and Hypoxic Conditions. *Dalton Trans.* **2022**, *51* (5), 1888–1900. https://doi.org/10.1039/D1DT02908H.

- (30) Xiao, Y.-F.; Chen, W.-C.; Chen, J.-X.; Lu, G.; Tian, S.; Cui, X.; Zhang, Z.; Chen, H.; Wan, Y.; Li, S.; Lee, C.-S. Amplifying Free Radical Generation of AIE Photosensitizer with Small Singlet—Triplet Splitting for Hypoxia-Overcoming Photodynamic Therapy. *ACS Appl. Mater. Interfaces* **2022**, *14* (4), 5112–5121. https://doi.org/10.1021/acsami.1c23797.
- (31) Schneider, L.; Kalt, M.; Koch, S.; Sithamparanathan, S.; Villiger, V.; Mattiat, J.; Kradolfer, F.; Slyshkina, E.; Luber, S.; Bonmarin, M.; Maake, C.; Spingler, B. BODIPY-Based Photothermal Agents with Excellent Phototoxic Indices for Cancer Treatment. *J. Am. Chem. Soc.* **2023**, *145* (8), 4534–4544. https://doi.org/10.1021/jacs.2c11650.
- (32) Deng, Z.; Li, H.; Chen, S.; Wang, N.; Liu, G.; Liu, D.; Ou, W.; Xu, F.; Wang, X.; Lei, D.; Lo, P.-C.; Li, Y. Y.; Lu, J.; Yang, M.; He, M.-L.; Zhu, G. Near-Infrared-Activated Anticancer Platinum(IV) Complexes Directly Photooxidize Biomolecules in an Oxygen-Independent Manner. *Nat. Chem.* **2023**, *15* (7), 930–939. https://doi.org/10.1038/s41557-023-01242-w.
- (33) Teng, K.-X.; Niu, L.-Y.; Yang, Q.-Z. Supramolecular Photosensitizer Enables Oxygen-Independent Generation of Hydroxyl Radicals for Photodynamic Therapy. *J. Am. Chem. Soc.* **2023**, *145* (7), 4081–4087. https://doi.org/10.1021/jacs.2c11868.
- (34) Li, R.; Hu, X.; Shang, F.; Wu, W.; Zhang, H.; Wang, Y.; Pan, J.; Shi, S.; Dong, C. Treatment of Triple Negative Breast Cancer by near Infrared Light Triggered Mild-Temperature Photothermal Therapy Combined with Oxygen-Independent Cytotoxic Free Radicals. *Acta Biomaterialia* **2022**, 148, 218–229. https://doi.org/10.1016/j.actbio.2022.06.011.
- (35) Dutta, D.; Wang, J.; Li, X.; Zhou, Q.; Ge, Z. Covalent Organic Framework Nanocarriers of Singlet Oxygen for Oxygen-Independent Concurrent Photothermal/Photodynamic Therapy to Ablate Hypoxic Tumors. *Small* **2022**, *18* (37), 2202369. https://doi.org/10.1002/smll.202202369.
- (36) Cao, F.; Wang, H.; Lu, N.; Zhang, P.; Huang, H. A Photoisomerizable Zinc (II) Complex Inhibits Microtubule Polymerization for Photoactive Therapy. *Angewandte Chemie* **2023**, *135* (14), e202301344. https://doi.org/10.1002/ange.202301344.
- (37) Chao, X.-J.; Huang, C.-H.; Tang, M.; Yan, Z.-Y.; Huang, R.; Li, Y.; Zhu, B.-Z. Unusual Enantioselective Cytoplasm-to-Nucleus Translocation and Photosensitization of the Chiral Ru(II) Cationic Complex via Simple Ion-Pairing with Lipophilic Weak Acid Counter-Anions. *Nucleic Acids Research* **2023**, *51* (7), 3041–3054. https://doi.org/10.1093/nar/gkad155.
- (38) Chen, Y.; Gu, L.; Ma, B.; Li, X.; Mei, Y.; Zhou, J.; Chong, Y.; Ma, M.; Zhang, M.; Wang, L.; Cheng, Y.; Wu, K.; Zeng, J.; Cheng, M.; Guo, P.; Zhang, P.; He, D. Photoactivatable Metal Organic Framework for Synergistic Ferroptosis and Photodynamic Therapy Using 450 Nm Laser. *Chemical Engineering Journal* **2023**, *454*, 140438. https://doi.org/10.1016/j.cej.2022.140438.
- (39) Liu, M.; Luo, Y.; Yan, J.; Xiong, X.; Xing, X.; Kim, J. S.; Zou, T. Photoactivation of Boronic Acid Prodrugs via a Phenyl Radical Mechanism: Iridium(III) Anticancer Complex as an Example. *J. Am. Chem. Soc.* **2023**, *145* (18), 10082–10091. https://doi.org/10.1021/jacs.3c00254.
- (40) Gandioso, A.; Izquierdo-García, E.; Mesdom, P.; Arnoux, P.; Demeubayeva, N.; Burckel, P.; Saubaméa, B.; Bosch, M.; Frochot, C.; Marchan, V.; Gasser, G. Ru(II)-Cyanine Complexes as Promising Photodynamic Photosensitizers for the Treatment of Hypoxic Tumours with Highly Penetrating 770 Nm Near-Infrared Light. *Chemistry A European J* 2023, e202301742. https://doi.org/10.1002/chem.202301742.
- (41) He, L.; Xu, F.; Li, Y.; Jin, H.; Lo, P.-C. Cupric-Ion-Promoted Fabrication of Oxygen-Replenishing Nanotherapeutics for Synergistic Chemo and Photodynamic Therapy against Tumor Hypoxia. *Acta Biomaterialia* **2023**, *162*, 57–71. https://doi.org/10.1016/j.actbio.2023.03.020.
- (42) He, M.; Wang, R.; Zhang, R.; Miao, P.; Wang, P.; Wei, Z.; Leng, X.; Li, Y.; Fan, J.; Peng, X.; Sun, W. The Construction of Polyphotocage Platform for Anticancer Photochemotherapy. *Adv Funct Materials* **2023**, *33* (26), 2300780. https://doi.org/10.1002/adfm.202300780.

- (43) Skelton, E.; Erasquin, U.; Sukul, A.; Zuercher, A.; White, J.; Bythell, B. J.; Cimatu, K. L. A. Visible Light-Assisted Coordination of a Rh(III)-BODIPY Complex to Guanine. *Inorg. Chem.* **2023**, *62* (8), 3368–3380. https://doi.org/10.1021/acs.inorgchem.2c03289.
- (44) Luo, T.; Yang, H.; Wang, R.; Pu, Y.; Cai, Z.; Zhao, Y.; Bi, Q.; Lu, J.; Jin, R.; Nie, Y.; Shuai, X. Bifunctional Cascading Nanozymes Based on Carbon Dots Promotes Photodynamic Therapy by Regulating Hypoxia and Glycolysis. *ACS Nano* **2023**, acsnano.3c03169. https://doi.org/10.1021/acsnano.3c03169.
- (45) Ma, Z.; Han, H.; Zhao, Y. Mitochondrial Dysfunction-Targeted Nanosystems for Precise Tumor Therapeutics. *Biomaterials* **2023**, 293, 121947. https://doi.org/10.1016/j.biomaterials.2022.121947.
- (46) Nwahara, N.; Abrahams, G.; Mack, J.; Prinsloo, E.; Nyokong, T. A Hypoxia Responsive Silicon Phthalocyanine Containing Naphthquinone Axial Ligands for Photodynamic Therapy Activity. *Journal of Inorganic Biochemistry* **2023**, 239, 112078. https://doi.org/10.1016/j.jinorgbio.2022.112078.
- (47) Olelewe, C.; Awuah, S. G. Mitochondria as a Target of Third Row Transition Metal-Based Anticancer Complexes. *Current Opinion in Chemical Biology* **2023**, *72*, 102235. https://doi.org/10.1016/j.cbpa.2022.102235.
- (48) Peng, J.; Du, K.; Sun, J.; Yang, X.; Wang, X.; Zhang, X.; Song, G.; Feng, F. Photocatalytic Generation of Hydrogen Radical (H·) with GSH for Photodynamic Therapy. *Angew Chem Int Ed* **2023**, *62* (9), e202214991. https://doi.org/10.1002/anie.202214991.
- (49) Rainho, M. D. A.; Siqueira, P. B.; De Amorim, Í. S. S.; Mencalha, A. L.; Thole, A. A. Mitochondria in Colorectal Cancer Stem Cells a Target in Drug Resistance. *Cancer Drug Resist* **2023**, *6* (2), 273–283. https://doi.org/10.20517/cdr.2022.116.
- (50) Rovira, A.; Ortega-Forte, E.; Hally, C.; Jordà-Redondo, M.; Abad-Montero, D.; Vigueras, G.; Martínez, J. I.; Bosch, M.; Nonell, S.; Ruiz, J.; Marchán, V. Exploring Structure—Activity Relationships in Photodynamic Therapy Anticancer Agents Based on Ir(III)-COUPY Conjugates. *J. Med. Chem.* **2023**, *66* (12), 7849–7867. https://doi.org/10.1021/acs.jmedchem.3c00189.
- (51) Silva, R. C.; Buzzá, H. H.; Ducas, E. S. A.; Oliveira, K. T.; Bagnato, V. S.; Souza, G. R. L.; Almeida, L. M.; Gonçalves, P. J. Synergic Vascular Photodynamic Activity by Methylene Blue-Curcumin Supramolecular Assembly. *Spectrochimica Acta Part A: Molecular and Biomolecular Spectroscopy* **2023**, *303*, 123281. https://doi.org/10.1016/j.saa.2023.123281.
- (52) Yang, Y.; Zou, X.; Sun, Y.; Chen, F.; Zhao, J.; Gou, S. Naphthalene Diimide-Functionalized Half-Sandwich Ru(II) Complexes as Mitochondria-Targeted Anticancer and Antimetastatic Agents. *Inorg. Chem.* **2023**, *62* (24), 9649–9660. https://doi.org/10.1021/acs.inorgchem.3c01125.
- (53) Sumit; Maravajjala, K. S.; Khanna, S.; Kachwal, V.; Swetha, K. L.; Manabala, S.; Chowdhury, R.; Roy, A.; Laskar, I. R. Rational Molecular Designing of Aggregation-Enhanced Emission (AEE) Active Red-Emitting Iridium(III) Complexes: Effect of Lipophilicity and Nanoparticle Encapsulation on Photodynamic Therapy Efficacy. ACS Appl. Bio Mater. 2023, 6 (4), 1445–1459. https://doi.org/10.1021/acsabm.2c00998.
- (54) Warszyńska, M.; Repetowski, P.; Dąbrowski, J. M. Photodynamic Therapy Combined with Immunotherapy: Recent Advances and Future Research Directions. *Coordination Chemistry Reviews* **2023**, *495*, 215350. https://doi.org/10.1016/j.ccr.2023.215350.
- (55) Weynand, J.; Episkopou, H.; Le Berre, G.; Gillard, M.; Dejeu, J.; Decottignies, A.; Defrancq, E.; Elias, B. Photo-Induced Telomeric DNA Damage in Human Cancer Cells. *RSC Chem. Biol.* **2022**, 3 (12), 1375–1379. https://doi.org/10.1039/D2CB00192F.
- (56) Zhou, J.-Y.; Shen, Q.-H.; Hong, X.-J.; Zhang, W.-Y.; Su, Q.; Li, W.-G.; Cheng, B.; Tan, C.-P.; Wu, T. Synergization of an Endoplasmic Reticulum-Targeted Iridium(III) Photosensitizer with PD-L1

- Inhibitor for Oral Squamous Cell Carcinoma Immunotherapy. *Chemical Engineering Journal* **2023**, *474*, 145516. https://doi.org/10.1016/j.cej.2023.145516.
- (57) Yuan, Z.; Wu, J.; Xiao, Y.; Yang, H.; Meng, S.; Dai, L.; Li, P.; Cai, K. A Photo-Therapeutic Nanocomposite with Bio-Responsive Oxygen Self-Supplying Combats Biofilm Infections and Inflammation from Drug-Resistant Bacteria. *Adv Funct Materials* **2023**, 2302908. https://doi.org/10.1002/adfm.202302908.
- (58) Zhang, L.; Wang, P.; Zhou, X.-Q.; Bretin, L.; Zeng, X.; Husiev, Y.; Polanco, E. A.; Zhao, G.; Wijaya, L. S.; Biver, T.; Le Dévédec, S. E.; Sun, W.; Bonnet, S. Cyclic Ruthenium-Peptide Conjugates as Integrin-Targeting Phototherapeutic Prodrugs for the Treatment of Brain Tumors. *J. Am. Chem. Soc.* 2023, 145 (27), 14963–14980. https://doi.org/10.1021/jacs.3c04855.
- (59) Zhdankin, G. I.; Grivin, V. P.; Plyusnin, V. F.; Tkachenko, P. A.; Vasilchenko, D. B.; Glebov, E. M. Chain Photosolvation of Trans, Trans, Trans-[PtlV(Py)2(N3)2(OH)2] Complex Prospective as a Light-Activated Antitumor Agent. *Mendeleev Communications* **2023**, *33* (1), 61–63. https://doi.org/10.1016/j.mencom.2023.01.019.
- (60) Knoll, J. D.; Albani, B. A.; Turro, C. Excited State Investigation of a New Ru(II) Complex for Dual Reactivity with Low Energy Light. *Chem. Commun. (Camb.)* **2015**, *51*, 8777–8780. https://doi.org/10.1039/c5cc01865j.
- (61) Knoll, J. D.; Turro, C. Control and Utilization of Ruthenium and Rhodium Metal Complex Excited States for Photoactivated Cancer Therapy. *Coord. Chem. Rev.* **2015**, *282*–*283*, 110–126. https://doi.org/10.1016/j.ccr.2014.05.018.
- (62) Bonnet, S. Why Develop Photoactivated Chemotherapy? *Dalton Transactions* **2018**, *47* (31), 10330–10343. https://doi.org/10.1039/C8DT01585F.
- (63) Roque III, J. A.; Cole, H. D.; Barrett, P. C.; Lifshits, L. M.; Hodges, R. O.; Kim, S.; Deep, G.; Francés-Monerris, A.; Alberto, M. E.; Cameron, C. G.; McFarland, S. A. Intraligand Excited States Turn a Ruthenium Oligothiophene Complex into a Light-Triggered Ubertoxin with Anticancer Effects in Extreme Hypoxia. *J. Am. Chem. Soc.* 2022, 144 (18), 8317–8336. https://doi.org/10.1021/jacs.2c02475.
- (64) White, J. K.; Schmehl, R. H.; Turro, C. An Overview of Photosubstitution Reactions of Ru(II) Imine Complexes and Their Application in Photobiology and Photodynamic Therapy. *Inorg. Chim. Acta* **2017**, *454* (Supplement C), 7–20. https://doi.org/10.1016/j.ica.2016.06.007.
- (65) Knoll, J. D.; Albani, B. A.; Turro, C. New Ru(II) Complexes for Dual Photoreactivity: Ligand Exchange and 1O2 Generation. *Accounts of Chemical Research* **2015**, *48* (8), 2280–2287. https://doi.org/10.1021/acs.accounts.5b00227.
- (66) Sun, Y.; Joyce, L. E.; Dickson, N. M.; Turro, C. Efficient DNA Photocleavage by [Ru(Bpy)2(Dppn)]2+ with Visible Light. *Chem. Commun.* **2010**, *46* (14), 2426–2428. https://doi.org/10.1039/B925574E.
- (67) Liu, Y.; Hammitt, R.; Lutterman, D. A.; Joyce, L. E.; Thummel, R. P.; Turro, C. Ru(II) Complexes of New Tridentate Ligands: Unexpected High Yield of Sensitized ¹O₂. *Inorganic Chemistry* **2009**, *48* (1), 375–385. https://doi.org/10.1021/ic801636u.
- (68) Zhao, R.; Hammitt, R.; Thummel, R. P.; Liu, Y.; Turro, C.; Snapka, R. M. Nuclear Targets of Photodynamic Tridentate Ruthenium Complexes. *Dalton Transactions* **2009**, No. 48, 10926. https://doi.org/10.1039/b913959a.
- (69) Yin, H.; Stephenson, M.; Gibson, J.; Sampson, E.; Shi, G.; Sainuddin, T.; Monro, S.; McFarland, S. A. In Vitro Multiwavelength PDT with 3IL States: Teaching Old Molecules New Tricks. *Inorganic Chemistry* **2014**, *53* (9), 4548–4559. https://doi.org/10.1021/ic5002368.
- (70) Albani, B. A.; Peña, B.; Leed, N. A.; de Paula, N. A. B. G.; Pavani, C.; Baptista, M. S.; Dunbar, K. R.; Turro, C. Marked Improvement in Photoinduced Cell Death by a New Tris-Heteroleptic

- Complex with Dual Action: Singlet Oxygen Sensitization and Ligand Dissociation. *Journal of the American Chemical Society* **2014**, *136* (49), 17095–17101. https://doi.org/10.1021/ja508272h.
- (71) Wachter, E.; Heidary, D. K.; Howerton, B. S.; Parkin, S.; Glazer, E. C. Light-Activated Ruthenium Complexes Photobind DNA and Are Cytotoxic in the Photodynamic Therapy Window. *Chem. Commun.* **2012**, *48* (77), 9649. https://doi.org/10.1039/c2cc33359g.
- (72) Bonnett, R. *Chemical Aspects of Photodynamic Therapy*; Advanced chemistry texts; Gordon and Breach Science Publishers: Amsterdam, The Netherlands, 2000.
- (73) Bonnet, S. Shifting the Light Activation of Metallodrugs to the Red and Near-Infrared Region in Anticancer Phototherapy. *Comments on Inorganic Chemistry* **2015**, *35* (4), 179–213. https://doi.org/10.1080/02603594.2014.979286.
- (74) Cuello-Garibo, J.-A.; Meijer, M. S.; Bonnet, S. To Cage or to Be Caged? The Cytotoxic Species in Ruthenium-Based Photoactivated Chemotherapy Is Not Always the Metal. *Chem. Commun.* **2017**, *53* (50), 6768–6771. https://doi.org/10.1039/C7CC03469E.
- (75) Azar, D. F.; Audi, H.; Farhat, S.; El-Sibai, M.; Abi-Habib, R. J.; Khnayzer, R. S. Phototoxicity of Strained Ru(II) Complexes: Is It the Metal Complex or the Dissociating Ligand? *Dalton Trans.* **2017**, *46* (35), 11529–11532. https://doi.org/10.1039/C7DT02255G.
- (76) Cole, H. D.; Roque, J. A.; Shi, G.; Lifshits, L. M.; Ramasamy, E.; Barrett, P. C.; Hodges, R. O.; Cameron, C. G.; McFarland, S. A. Anticancer Agent with Inexplicable Potency in Extreme Hypoxia: Characterizing a Light-Triggered Ruthenium Ubertoxin. *J. Am. Chem. Soc.* **2022**, *144* (22), 9543–9547. https://doi.org/10.1021/jacs.1c09010.
- (77) Sun, Y.; Heidary, D. K.; Zhang, Z.; Richards, C. I.; Glazer, E. C. Bacterial Cytological Profiling Reveals the Mechanism of Action of Anticancer Metal Complexes. *Mol. Pharm.* **2018**, *15* (8), 3404–3416. https://doi.org/10.1021/acs.molpharmaceut.8b00407.
- (78) Albani, B. A.; Durr, C. B.; Turro, C. Selective Photoinduced Ligand Exchange in a New Tris—Heteroleptic Ru(II) Complex. *The Journal of Physical Chemistry A* **2013**, *117* (50), 13885–13892. https://doi.org/10.1021/jp4085684.
- (79) Knoll, J. D.; Albani, B. A.; Durr, C. B.; Turro, C. Unusually Efficient Pyridine Photodissociation from Ru(II) Complexes with Sterically Bulky Bidentate Ancillary Ligands. *The Journal of Physical Chemistry A* **2014**, *118* (45), 10603–10610. https://doi.org/10.1021/jp5057732.
- (80) Arora, K.; White, J. K.; Sharma, R.; Mazumder, S.; Martin, P. D.; Schlegel, H. B.; Turro, C.; Kodanko, J. J. Effects of Methyl Substitution in Ruthenium Tris(2-Pyridylmethyl)Amine Photocaging Groups for Nitriles. *Inorganic Chemistry* 2016, 55 (14), 6968–6979. https://doi.org/10.1021/acs.inorgchem.6b00650.
- (81) Huisman, M.; White, J. K.; Lewalski, V. G.; Podgorski, I.; Turro, C.; Kodanko, J. J. Caging the Uncageable: Using Metal Complex Release for Photochemical Control over Irreversible Inhibition. *Chemical Communications* **2016**, *52* (85), 12590–12593. https://doi.org/10.1039/C6CC07083C.
- (82) Li, A.; Yadav, R.; White, J. K.; Herroon, M. K.; Callahan, B. P.; Podgorski, I.; Turro, C.; Scott, E. E.; Kodanko, J. J. Illuminating Cytochrome P450 Binding: Ru(II)-Caged Inhibitors of CYP17A1. *Chem. Commun.* **2017**, *53* (26), 3673–3676. https://doi.org/10.1039/C7CC01459G.
- (83) Arora, K.; Herroon, M.; Al-Afyouni, M. H.; Toupin, N. P.; Rohrabaugh, T. N.; Loftus, L. M.; Podgorski, I.; Turro, C.; Kodanko, J. J. Catch and Release Photosensitizers: Combining Dual-Action Ruthenium Complexes with Protease Inactivation for Targeting Invasive Cancers. *J. Am. Chem. Soc.* **2018**, *140* (43), 14367–14380. https://doi.org/10.1021/jacs.8b08853.
- (84) Li, A.; Turro, C.; Kodanko, J. J. Ru(II) Polypyridyl Complexes Derived from Tetradentate Ancillary Ligands for Effective Photocaging. *Accounts of Chemical Research* **2018**, *51* (6), 1415–1421. https://doi.org/10.1021/acs.accounts.8b00066.

- (85) Li, A.; Turro, C.; Kodanko, J. J. Ru(II) Polypyridyl Complexes as Photocages for Bioactive Compounds Containing Nitriles and Aromatic Heterocycles. *Chem. Commun.* **2018**, *54* (11), 1280–1290. https://doi.org/10.1039/C7CC09000E.
- (86) Nisbett, K.; Tu, Y.-J.; Turro, C.; Kodanko, J. J.; Schlegel, H. B. DFT Investigation of Ligand Photodissociation in [Rull(Tpy)(Bpy)(Py)]2+ and [Rull(Tpy)(Me2bpy)(Py)]2+ Complexes. *Inorganic Chemistry* **2018**, *57* (1), 231–240. https://doi.org/10.1021/acs.inorgchem.7b02398.
- (87) Rohrabaugh, T. N.; Rohrabaugh, A. M.; Kodanko, J. J.; White, J. K.; Turro, C. Photoactivation of Imatinib–Antibody Conjugate Using Low-Energy Visible Light from Ru(II)-Polypyridyl Cages. *Chem. Commun.* **2018**, *54* (41), 5193–5196. https://doi.org/10.1039/C8CC01348A.
- (88) Bahreman, A.; Limburg, B.; Siegler, M. A.; Bouwman, E.; Bonnet, S. Spontaneous Formation in the Dark, and Visible Light-Induced Cleavage, of a Ru–S Bond in Water: A Thermodynamic and Kinetic Study. *Inorganic Chemistry* **2013**, *52* (16), 9456–9469. https://doi.org/10.1021/ic401105v.
- (89) Bahreman, A.; Rabe, M.; Kros, A.; Bruylants, G.; Bonnet, S. Binding of a Ruthenium Complex to a Thioether Ligand Embedded in a Negatively Charged Lipid Bilayer: A Two-Step Mechanism. Chemistry - A European Journal 2014, 20 (24), 7429–7438. https://doi.org/10.1002/chem.201400377.
- (90) Göttle, A. J.; Alary, F.; Boggio-Pasqua, M.; Dixon, I. M.; Heully, J.-L.; Bahreman, A.; Askes, S. H. C.; Bonnet, S. Pivotal Role of a Pentacoordinate ³MC State on the Photocleavage Efficiency of a Thioether Ligand in Ruthenium(II) Complexes: A Theoretical Mechanistic Study. *Inorganic Chemistry* **2016**, *55* (9), 4448–4456. https://doi.org/10.1021/acs.inorgchem.6b00268.
- (91) Cuello-Garibo, J.-A.; Pérez-Gallent, E.; van der Boon, L.; Siegler, M. A.; Bonnet, S. Influence of the Steric Bulk and Solvent on the Photoreactivity of Ruthenium Polypyridyl Complexes Coordinated to L-Proline. *Inorganic Chemistry* 2017, *56* (9), 4818–4828. https://doi.org/10.1021/acs.inorgchem.6b02794.
- (92) Sun, W.; Wen, Y.; Thiramanas, R.; Chen, M.; Han, J.; Gong, N.; Wagner, M.; Jiang, S.; Meijer, M. S.; Bonnet, S.; Butt, H.-J.; Mailänder, V.; Liang, X.-J.; Wu, S. Red-Light-Controlled Release of Drug-Ru Complex Conjugates from Metallopolymer Micelles for Phototherapy in Hypoxic Tumor Environments. *Adv. Funct. Mater.* 2018, 28 (39), 1804227. https://doi.org/10.1002/adfm.201804227.
- (93) Meijer, M. S.; Talens, V. S.; Hilbers, M. F.; Kieltyka, R. E.; Brouwer, A. M.; Natile, M. M.; Bonnet, S. NIR-Light-Driven Generation of Reactive Oxygen Species Using Ru(II)-Decorated Lipid-Encapsulated Upconverting Nanoparticles. *Langmuir* **2019**, *35* (37), 12079–12090. https://doi.org/10.1021/acs.langmuir.9b01318.
- (94) Havrylyuk, D.; Hachey, A. C.; Fenton, A.; Heidary, D. K.; Glazer, E. C. Ru(II) Photocages Enable Precise Control over Enzyme Activity with Red Light. *Nat Commun* **2022**, *13* (1), 3636. https://doi.org/10.1038/s41467-022-31269-5.
- (95) Ryan, R. T.; Havrylyuk, D.; Stevens, K. C.; Moore, L. H.; Parkin, S.; Blackburn, J. S.; Heidary, D. K.; Selegue, J. P.; Glazer, E. C. Biological Investigations of Ru(II) Complexes with Diverse β-Diketone Ligands. *Eur. J. Inorg. Chem.* 2021, 2021 (35), 3611–3621. https://doi.org/10.1002/ejic.202100468.
- (96) Huang, H.; Banerjee, S.; Qiu, K.; Zhang, P.; Blacque, O.; Malcomson, T.; Paterson, M. J.; Clarkson, G. J.; Staniforth, M.; Stavros, V. G.; Gasser, G.; Chao, H.; Sadler, P. J. Targeted Photoredox Catalysis in Cancer Cells. *Nat. Chem.* **2019**, *11* (11), 1041–1048. https://doi.org/10.1038/s41557-019-0328-4.
- (97) Baptista, M. S.; Cadet, J.; Di Mascio, P.; Ghogare, A. A.; Greer, A.; Hamblin, M. R.; Lorente, C.; Nunez, S. C.; Ribeiro, M. S.; Thomas, A. H.; Vignoni, M.; Yoshimura, T. M. Type I and Type II

- Photosensitized Oxidation Reactions: Guidelines and Mechanistic Pathways. *Photochemistry and Photobiology* **2017**, 93 (4), 912–919. https://doi.org/10.1111/php.12716.
- (98) Shi, G.; Monro, S.; Hennigar, R.; Colpitts, J.; Fong, J.; Kasimova, K.; Yin, H.; DeCoste, R.; Spencer, C.; Chamberlain, L.; Mandel, A.; Lilge, L.; McFarland, S. A. Ru(II) Dyads Derived from α-Oligothiophenes: A New Class of Potent and Versatile Photosensitizers for PDT. *Coord. Chem. Rev.* 2015, 282–283, 127–138. https://doi.org/10.1016/j.ccr.2014.04.012.
- (99) Lifshits, L. M.; Roque, J. A.; Cole, H. D.; Thummel, R. P.; Cameron, C. G.; McFarland, S. A. NIR-Absorbing Ru II Complexes Containing α-Oligothiophenes for Applications in Photodynamic Therapy. *ChemBioChem* **2020**, *21*, 3594–3607. https://doi.org/10.1002/cbic.202000419.
- (100) Luis, E. T.; Ball, G. E.; Gilbert, A.; Iranmanesh, H.; Newdick, C. W.; Beves, J. E. Efficient Microwave-Assisted Synthesis and Characterization of Key Ruthenium(II) Polypyridyl Complexes [Ru(Bpy) 3](PF 6) 2, [Ru(Phen) 3](PF 6) 2, [Ru(Bpy) 2 (Phen)](PF 6) 2 and [Ru(Phen) 2 (Bpy)](PF 6) 2. Journal of Coordination Chemistry 2016, 69 (11–13), 1686–1694. https://doi.org/10.1080/00958972.2016.1194404.
- (101) Sullivan, B.; Salmon, D.; Meyer, T. Mixed Phosphine 2,2'-Bipyridine Complexes of Ruthenium. **1978**, *17*, 3334–3341.
- (102) Wang, Z. Comprehensive Organic Name Reactions and Reagents; John Wiley & Sons, Inc.: Hoboken, NJ, USA, 2010. https://doi.org/10.1002/9780470638859.
- (103) Ghosh, G.; Colón, K. L.; Fuller, A.; Sainuddin, T.; Bradner, E.; McCain, J.; Monro, S. M. A.; Yin, H.; Hetu, M. W.; Cameron, C. G.; McFarland, S. A. Cyclometalated Ruthenium(II) Complexes Derived from α-Oligothiophenes as Highly Selective Cytotoxic or Photocytotoxic Agents. *Inorg. Chem.* 2018, *57* (13), 7694–7712. https://doi.org/10.1021/acs.inorgchem.8b00689.
- (104) Chen, R.; Yang, X.; Tian, H.; Wang, X.; Hagfeldt, A.; Sun, L. Effect of Tetrahydroquinoline Dyes Structure on the Performance of Organic Dye-Sensitized Solar Cells. *Chem. Mater.* **2007**, *19* (16), 4007–4015. https://doi.org/10.1021/cm070617g.
- (105) Casida, M. E. Time–Dependent Density Functional Response Theory of Molecular Systems: Theory, Computational Methods, and Functionals. In *Recent developments and applications of modern density functional theory*; Seminario, J. M., Ed.; Theoretical and computational chemistry; Elsevier: Amsterdam; Netherlands, 1996; pp 155–192.
- (106) Frisch, M. J.; Trucks, G. W.; Schlegel, H. B.; Scuseria, G. E.; Robb, M. A.; Cheeseman, J. R.; Scalmani, G.; Barone, V.; Petersson, G. A.; Nakatsuji, H.; Li, X.; Caricato, M.; Marenich, A. V.; Bloino, J.; Janesko, B. G.; Gomperts, R.; Mennucci, B.; Hratchian, H. P.; Ortiz, J. V.; Izmaylov, A. F.; Sonnenberg, J. L.; Williams-Young, D.; Ding, F.; Lipparini, F.; Egidi, F.; Goings, J.; Peng, B.; Petrone, A.; Henderson, T.; Ranasinghe, D.; Zakrzewski, V. G.; Gao, J.; Rega, N.; Zheng, G.; Liang, W.; Hada, M.; Ehara, M.; Toyota, K.; Fukuda, R.; Hasegawa, J.; Ishida, M.; Nakajima, T.; Honda, Y.; Kitao, O.; Nakai, H.; Vreven, T.; Throssell, K.; Montgomery, J. A., Jr.; Peralta, J. E.; Ogliaro, F.; Bearpark, M. J.; Heyd, J. J.; Brothers, E. N.; Kudin, K. N.; Staroverov, V. N.; Keith, T. A.; Kobayashi, R.; Normand, J.; Raghavachari, K.; Rendell, A. P.; Burant, J. C.; Iyengar, S. S.; Tomasi, J.; Cossi, M.; Millam, J. M.; Klene, M.; Adamo, C.; Cammi, R.; Ochterski, J. W.; Martin, R. L.; Morokuma, K.; Farkas, O.; Foresman, J. B.; Fox, D. J. *Gaussian 16 Revision C.01*; 2016.
- (107) Ponte, F.; Alberto, M. E.; De Simone, B. C.; Russo, N.; Sicilia, E. Photophysical Exploration of Dual-Approach Pt^{II}–BODIPY Conjugates: Theoretical Insights. *Inorg. Chem.* **2019**, *58* (15), 9882–9889. https://doi.org/10.1021/acs.inorgchem.9b01002.
- (108) Alberto, M. E.; Francés-Monerris, A. A Multiscale Free Energy Method Reveals an Unprecedented Photoactivation of a Bimetallic Os(II)–Pt(II) Dual Anticancer Agent. *Phys. Chem. Chem. Phys.* **2022**, *24* (32), 19584–19594. https://doi.org/10.1039/D2CP02128E.

- (109) Alberto, M. E.; Russo, N.; Adamo, C. Synergistic Effects of Metals in a Promising Ru^{II}–Pt ^{II} Assembly for a Combined Anticancer Approach: Theoretical Exploration of the Photophysical Properties. *Chemistry A European Journal* **2016**, *22* (27), 9162–9168. https://doi.org/10.1002/chem.201601089.
- (110) Alberto, M. E.; Pirillo, J.; Russo, N.; Adamo, C. Theoretical Exploration of Type I/Type II Dual Photoreactivity of Promising Ru(II) Dyads for PDT Approach. *Inorg. Chem.* **2016**, *55* (21), 11185–11192. https://doi.org/10.1021/acs.inorgchem.6b01782.
- (111) Bertini, L.; Alberto, M. E.; Arrigoni, F.; Vertemara, J.; Fantucci, P.; Bruschi, M.; Zampella, G.; De Gioia, L. On the Photochemistry of Fe₂(Edt)(CO)₄(PMe ₃)₂, a [FeFe]-Hydrogenase Model: A DFT/TDDFT Investigation. *Int J Quantum Chem* **2018**, *118* (9), e25537. https://doi.org/10.1002/gua.25537.
- (112) Alberto, M. E.; Adamo, C. Synergistic Effects in Pt^{II}-Porphyrinoid Dyes as Candidates for a Dual-Action Anticancer Therapy: A Theoretical Exploration. *Chemistry A European Journal* **2017**, 23 (60), 15124–15132. https://doi.org/10.1002/chem.201702876.
- (113) Francés-Monerris, A.; Magra, K.; Darari, M.; Cebrián, C.; Beley, M.; Domenichini, E.; Haacke, S.; Pastore, M.; Assfeld, X.; Gros, P. C.; Monari, A. Synthesis and Computational Study of a Pyridylcarbene Fe(II) Complex: Unexpected Effects of *Facl Mer* Isomerism in Metal-to-Ligand Triplet Potential Energy Surfaces. *Inorg. Chem.* 2018, 57 (16), 10431–10441. https://doi.org/10.1021/acs.inorgchem.8b01695.
- (114) Alberto, M. E.; Mazzone, G.; Regina, C.; Russo, N.; Sicilia, E. Theoretical Exploration of the Photophysical Properties of Two-Component Ru^{II}—Porphyrin Dyes as Promising Assemblies for a Combined Antitumor Effect. *Dalton Trans.* **2020**, *49* (36), 12653–12661. https://doi.org/10.1039/D0DT02197K.
- (115) Adamo, C.; Barone, V. Toward Reliable Density Functional Methods without Adjustable Parameters: The PBE0 Model. *The Journal of Chemical Physics* **1999**, *110* (13), 6158–6170. https://doi.org/10.1063/1.478522.
- (116) Andrae, D.; Häußermann, U.; Dolg, M.; Stoll, H.; Preuß, H. Energy-Adjusted Ab Initio Pseudopotentials for the Second and Third Row Transition Elements. *Theoret. Chim. Acta* **1990**, 77 (2), 123–141. https://doi.org/10.1007/BF01114537.
- (117) Cossi, M.; Barone, V. Solvent Effect on Vertical Electronic Transitions by the Polarizable Continuum Model. *The Journal of Chemical Physics* **2000**, *112* (5), 2427–2435. https://doi.org/10.1063/1.480808.
- (118) Tomasi, J.; Mennucci, B.; Cammi, R. Quantum Mechanical Continuum Solvation Models. *Chemical Reviews* **2005**, *105* (8), 2999–3094. https://doi.org/10.1021/cr9904009.
- (119) Cossi, M.; Rega, N.; Scalmani, G.; Barone, V. Energies, Structures, and Electronic Properties of Molecules in Solution with the C-PCM Solvation Model. *J. Comput. Chem.* **2003**, *24* (6), 669–681. https://doi.org/10.1002/jcc.10189.
- (120) Hirata, S.; Head-Gordon, M. Time-Dependent Density Functional Theory within the Tamm–Dancoff Approximation. *Chemical Physics Letters* **1999**, *314* (3–4), 291–299. https://doi.org/10.1016/S0009-2614(99)01149-5.
- (121) Peach, M. J. G.; Williamson, M. J.; Tozer, D. J. Influence of Triplet Instabilities in TDDFT. *J. Chem. Theory Comput.* **2011**, 7 (11), 3578–3585. https://doi.org/10.1021/ct200651r.
- (122) Skripnikov, L. Chemissan, 43rd ed.; Vol. 4.
- (123) Plasser, F. TheoDORE: A Toolbox for a Detailed and Automated Analysis of Electronic Excited State Computations. *The Journal of Chemical Physics* **2020**, *152* (8), 084108. https://doi.org/10.1063/1.5143076.

- (124) Scherrer, R. A.; Howard, S. M. Use of Distribution Coefficients in Quantitative Structure-Activity Relations. *J. Med. Chem.* **1977**, *20* (1), 53–58. https://doi.org/10.1021/jm00211a010.
- (125) Alberto, M. E.; De Simone, B. C.; Mazzone, G.; Sicilia, E.; Russo, N. The Heavy Atom Effect on Zn(II) Phthalocyanine Derivatives: A Theoretical Exploration of the Photophysical Properties. *Physical Chemistry Chemical Physics* 2015, 17 (36), 23595–23601. https://doi.org/10.1039/C5CP03833B.
- (126) DeRosa, M. Photosensitized Singlet Oxygen and Its Applications. *Coordination Chemistry Reviews* **2002**, 233–234, 351–371. https://doi.org/10.1016/S0010-8545(02)00034-6.
- (127) Young, R. C.; Meyer, T. J.; Whitten, D. G. Electron Transfer Quenching of Excited States of Metal Complexes. J. Am. Chem. Soc. 1976, 98 (1), 286–287. https://doi.org/10.1021/ja00417a073.
- (128) Becker, R. S.; Seixas de Melo, J.; Maçanita, A. L.; Elisei, F. Comprehensive Evaluation of the Absorption, Photophysical, Energy Transfer, Structural, and Theoretical Properties of α-Oligothiophenes with One to Seven Rings. *J. Phys. Chem.* **1996**, *100*, 18683–18695. https://doi.org/10.1021/jp960852e.
- (129) Juris, A.; Balzani, V.; Barigelletti, F.; Campagna, S.; Belser, P.; von Zelewsky, A. Ru(II) Polypyridine Complexes: Photophysics, Photochemistry, Eletrochemistry, and Chemiluminescence. *Coordination Chemistry Reviews* **1988**, *84*, 85–277. https://doi.org/10.1016/0010-8545(88)80032-8.
- (130) Elfring, W. H.; Crosby, G. A. Excited States of Mixed-Ligand Chelates of Ruthenium(II). Quantum Yield and Decay Time Measurements. *J. Am. Chem. Soc.* **1981**, *103* (10), 2683–2687. https://doi.org/10.1021/ja00400a032.
- (131) Hissler, M.; Connick, W. B.; Geiger, D. K.; McGarrah, J. E.; Lipa, D.; Lachicotte, R. J.; Eisenberg, R. Platinum Diimine Bis(Acetylide) Complexes: Synthesis, Characterization, and Luminescence Properties. *Inorg. Chem.* **2000**, *39* (3), 447–457. https://doi.org/10.1021/ic991250n.
- (132) Lincoln, R.; Kohler, L.; Monro, S.; Yin, H.; Stephenson, M.; Zong, R.; Chouai, A.; Dorsey, C.; Hennigar, R.; Thummel, R. P.; McFarland, S. A. Exploitation of Long-Lived 3IL Excited States for Metal–Organic Photodynamic Therapy: Verification in a Metastatic Melanoma Model. *J. Am. Chem. Soc.* **2013**, *135* (45), 17161–17175. https://doi.org/10.1021/ja408426z.
- (133) DeRosa, M. C.; Crutchley, R. J. Photosensitized Singlet Oxygen and Its Applications. *Coord. Chem. Rev.* **2002**, *233*–*234*, 351–371. https://doi.org/10.1016/S0010-8545(02)00034-6.
- (134) Montalti, M.; Credi, A.; Prodi, L.; Gandolfi, M. T. *Handbook of Photochemistry*; CRC Press, 2006. https://doi.org/10.1201/9781420015195.
- (135) Lifshits, L. M.; Roque III, J. A.; Konda, P.; Monro, S.; Cole, H. D.; von Dohlen, D.; Kim, S.; Deep, G.; Thummel, R. P.; Cameron, C. G.; Gujar, S.; McFarland, S. A. Near-Infrared Absorbing Ru(II) Complexes Act as Immunoprotective Photodynamic Therapy (PDT) Agents against Aggressive Melanoma. *Chem. Sci.* **2020**, *11* (43), 11740–11762. https://doi.org/10.1039/D0SC03875J.
- (136) Chettri, A.; Roque, J. A.; Schneider, K. R. A.; Cole, H. D.; Cameron, C. G.; McFarland, S. A.; Dietzek, B. It Takes Three to Tango: The Length of the Oligothiophene Chain Determines the Nature of the Long-Lived Excited State and the Resulting Photocytotoxicity of a Ruthenium(II) Photodrug. *ChemPhotoChem* **2021**, *5* (5), 421–425. https://doi.org/10.1002/cptc.202000283.
- (137) McCain, J.; Colón, K. L.; Barrett, P. C.; Monro, S. M. A.; Sainuddin, T.; Roque III, J.; Pinto, M.; Yin, H.; Cameron, C. G.; McFarland, S. A. Photophysical Properties and Photobiological Activities of Ruthenium(II) Complexes Bearing π-Expansive Cyclometalating Ligands with Thienyl Groups. *Inorg. Chem.* **2019**, *58* (16), 10778–10790. https://doi.org/10.1021/acs.inorgchem.9b01044.
- (138) Monro, S.; Cameron, C. G.; Zhu, X.; Colón, K. L.; Yin, H.; Sainuddin, T.; Hetu, M.; Pinto, M.; Fuller, A.; Bennett, L.; Roque, J.; Sun, W.; McFarland, S. A. Synthesis, Characterization and

- Photobiological Studies of Ru(II) Dyads Derived from α-Oligothiophene Derivatives of 1,10-Phenanthroline. *Photochem. Photobiol.* **2019**, 95 (1), 267–279. https://doi.org/10.1111/php.13012.
- (139) Ghosh, G.; Colón, K. L.; Fuller, A.; Sainuddin, T.; Bradner, E.; McCain, J.; Monro, S. M. A.; Yin, H.; Hetu, M. W.; Cameron, C. G.; McFarland, S. A. Cyclometalated Ruthenium(II) Complexes Derived from α-Oligothiophenes as Highly Selective Cytotoxic or Photocytotoxic Agents. *Inorg. Chem.* **2018**, *57* (13), 7694–7712. https://doi.org/10.1021/acs.inorgchem.8b00689.
- (140) Diaz, A. F.; Crowley, J.; Bargon, J.; Gardini, G. P.; Torrance, J. B. Electrooxidation of Aromatic Oligomers and Conducting Polymers. *Journal of Electroanalytical Chemistry and Interfacial Electrochemistry* **1981**, *121*, 355–361. https://doi.org/10.1016/S0022-0728(81)80592-X.
- (141) Tokel-Takvoryan, N. E.; Hemingway, R. E.; Bard, A. J. Electrogenerated Chemiluminescence. XIII. Electrochemical and Electrogenerated Chemiluminescence Studies of Ruthenium Chelates. *J. Am. Chem. Soc.* **1973**, *95* (20), 6582–6589. https://doi.org/10.1021/ja00801a011.
- (142) Camarada, M. B.; Jaque, P.; Díaz, F. R.; del Valle, M. A. Oxidation Potential of Thiophene Oligomers: Theoretical and Experimental Approach. *J. Polym. Sci. B Polym. Phys.* **2011**, *49* (24), 1723–1733. https://doi.org/10.1002/polb.22360.
- (143) Vlcek, A. A.; Dodsworth, E. S.; Pietro, W. J.; Lever, A. B. P. Excited State Redox Potentials of Ruthenium Diimine Complexes; Correlations with Ground State Redox Potentials and Ligand Parameters. *Inorg. Chem.* 1995, 34 (7), 1906–1913. https://doi.org/10.1021/ic00111a043.
- (144) Chettri, A.; Schneider, K. R. A.; Cole, H. D.; Roque, J. A.; Cameron, C. G.; McFarland, S. A.; Dietzek, B. String-Attached Oligothiophene Substituents Determine the Fate of Excited States in Ruthenium Complexes for Photodynamic Therapy. *J. Phys. Chem. A* **2021**, *125* (32), 6985–6994. https://doi.org/10.1021/acs.jpca.1c04900.